Surface roughness effects on transonic aircraft performance: Experimental/numerical comparisons

David Hue, Aurelia Cartieri, Ilias Petropoulos

Aerospace Science and Technology 154 (2024) 109507

Contents lists available at ScienceDirect

Aerospace Science and Technology

journal homepage: www.elsevier.com/locate/aescte

Surface roughness effects on transonic aircraft performance: Experimental/numerical comparisons

David Hue [a], Aurélia Cartieri [b], Ilias Petropoulos [a,*]

[a] Department of Aerodynamics, Aeroelasticity, Acoustics, ONERA – The French Aerospace Lab, 921290 Meudon, France
[b] Wind Tunnel Division, ONERA – The French Aerospace Lab, 73500 Modane, France

ARTICLE INFO

Communicated by Mr Damiano Casalino.

Keywords:
Aircraft
Drag
Prediction
Surface roughness
Wind tunnel
Flight

ABSTRACT

This work highlights the necessity of taking into account surface roughness when conducting experimental tests, and when using numerical simulations to precisely calculate the turbulent lift and drag of wind-tunnel models or real aircraft in transonic conditions. The present article is a continuation of "Turbulent drag induced by low surface roughness at transonic speeds: Experimental/numerical comparisons," Physics of Fluids, Vol. 32, 045108 (2020) by Hue and Molton. The outcomes of this former study, which was focused on flat plate samples, are here applied to a three-dimensional aircraft configuration: the Common Research Model used as a reference in the recent international Drag Prediction Workshops. Experimental campaigns have been performed in the largest ONERA wind tunnels S1MA and S2MA involving models with average surface roughness heights *Ra* close to 0.5 micrometers, wingspans up to 3.5 meters, Mach and Reynolds numbers up to 0.95 and 5 million respectively. Reynolds-averaged Navier–Stokes computations based on the wind-tunnel tests have then been carried out, using the equivalent sand-grain roughness height approach as well as a Musker-type correlation to determine relevant k_s values. The results of both the experimental and numerical campaigns have demonstrated that the aerodynamic coefficients of the aircraft can be significantly affected by the surface roughness, even with roughness Reynolds numbers k_s^+ potentially below the usual threshold values sometimes considered in engineering applications (i.e. in the order of 3.5 to 5). In particular, the surface roughness effects on lift and drag have been studied using far-field analyses to evaluate the responses of friction, viscous pressure, wave and lift-induced drag components. Finally, the numerical studies have been extended to the full-scale geometry in flight conditions in order to assess the roughness effects and potential gains in realistic aircraft operating conditions.

1. Introduction

Wind tunnel and flight experiments are indispensable in transonic aircraft design, as Computational Fluid Dynamics (CFD) simulations are still undoubtedly far from being able to completely cover their role throughout the certification process and across the flight envelope. Even if great progress is made through outstandingly fine-resolution calculations carried out on ever more powerful supercomputers, the numerical and experimental approaches should remain complementary. Nonetheless, direct comparisons of results between the two are not always straightforward due to each approach involving a multitude of particularities not only in physics but also in terms of numerical approximation, assumptions or modelling. As such, the aeronautics community is continuously searching for ways of refining its capacity to compare simulations against wind-tunnel or flight-test data, a subject which relies on the understanding of the precise influence of mechanisms introducing discrepancies in this comparison.

The starting point of this work was the observation of a significant difference between the numerical drag and the corrected drag obtained in the large ONERA S1MA wind tunnel [1] for the Common Research Model (CRM) [2] civil aircraft configuration used in recent international Drag Prediction Workshops (DPW) [3,4]. Back in 2018, the specific choice of the two-equation k-ω SST model of Menter [5] with the dissipation wall treatment proposed by Wilcox in [6] (where ω is a function depending on a pseudo-roughness height k^+, and $k^+ \sim 5$ for smooth walls) was found to noticeably improve the agreement between the CFD and experimental drag polars. Since the S1MA data was already corrected for wall and support system effects, the aforementioned observation sparked the suspicion of the surface roughness of the wind-tunnel model being responsible for the drag overproduction compared to the infinitely-smooth geometry used in the initial

* Corresponding author.
E-mail addresses: david.hue@onera.fr (D. Hue), aurelia.cartieri@onera.fr (A. Cartieri), ilias.petropoulos@onera.fr (I. Petropoulos).

https://doi.org/10.1016/j.ast.2024.109507
Received 22 February 2024; Received in revised form 19 July 2024; Accepted 17 August 2024
Available online 17 August 2024

Nomenclature

alpha	angle of attack
b	wingspan
c	wing chord
CDf	friction drag coefficient
CDff	far-field drag coefficient
CDi	lift-induced drag coefficient
CDnf	near-field drag coefficient
CDp	pressure drag coefficient
CDsp	spurious drag coefficient
CDv	viscous drag coefficient
CDvp	viscous pressure drag coefficient
CDw	wave drag coefficient
Cf	skin friction coefficient
CL	lift coefficient
CM	pitching moment coefficient
Cp	pressure coefficient
dc	drag count (1×10^{-4})
k_s	equivalent sand-grain height
k_s^+	roughness Reynolds number
Ma	Mach number
Ra	average roughness height
Re	Reynolds number
Sref	reference surface area
U_τ	friction velocity
Y^+	normalized first cell height
η	fraction of span

simulations. Shortly after, a second wind-tunnel-test campaign involving Pressure-Sensitive Paint (PSP) techniques seemed to reinforce this lead.

Effects due to surface roughness have been found to influence flow dynamics in a broad range of applications. In applied aerodynamics, and especially in aeronautics applications, surface roughness introduces notable effects on drag, heat transfer and turbulent mixing characteristics. These aspects are therefore of common interest in applications such as icing, or in turbomachinery and in particular turbine components [7] (e.g. additive manufacturing [8]). The surface roughness itself can be resolved in the frame of high-fidelity physical analyses [9], but many approaches aim at representing the main effects due to surface roughness through appropriate models. Refined models such as discrete element methods (cf. [10] and references therein), are still being investigated with the further view of a straightforward inclusion of surface roughness effects in applied studies. Nonetheless, simpler models based on an equivalent sand-grain height approach remain commonly in use for engineering applications [11–13].

Hue and Molton [14] investigated an engineering-oriented correlation in conjunction with an equivalent sand-grain height model in terms of its capacity in representing the leading surface roughness effects on drag assessment studies. Experimental measurements were obtained in a relatively small research wind tunnel in order to consider a large number of samples and conditions. The study itself was motivated by the aforementioned applied aerodynamics context involving comparisons between wind-tunnel experiments and numerical simulations of the CRM geometry. The study included a discussion of the work of pioneers on the subject, such as Nikuradse [15], Colebrook [16], Moody [17], as well as recent reviews and numerical studies involving large eddy simulations or direct numerical simulation strategies [18–21]. Other broader-spectrum reviews on the subject of surface roughness resolution and modelling have recently been presented by Kadivar et al. [13] and by Chung et al. [22]. The study of Hue and Molton [14] was mainly based on the concept of equivalent sand-grain roughness height k_s and showed the comparison between the micro-drags measured in the ONERA S8Ch wind tunnel (see Fig. 1) for a dozen flat plate samples of different roughness characteristics and the associated drags computed using Reynolds-averaged Navier-Stokes (RANS) simulations. These simulations were coupled with a correlation adapted from the one proposed by Musker [23], as $k_s = Rq(1 + a^*Sp)(1 + b^*Sk^*Ku)$, where *Rq* is the root-mean-square (RMS) roughness height, *Sk* and *Ku* are the skewness and kurtosis coefficients and *Sp* the slope parameter (see Table 1). This correlation has the advantage of emphasizing the existence and importance of subtler parameters, beyond the average

Table 1
Main roughness parameters and their definitions.

$Ra = \frac{1}{l_r}\int_0^{l_r} \lvert Z(X)\rvert dX$	$Rq = \sqrt{\frac{1}{l_r}\int_0^{l_r} Z^2(X)dX}$	$Rz = \frac{1}{5}\sum_1^5 (Rp(i) + \lvert Rv(i)\rvert)$
$Sk = \frac{1}{Rq^3}\left[\frac{1}{l_r}\int_0^{l_r} Z^3(X)dX\right]$	$Ku = \frac{1}{Rq^4}\left[\frac{1}{l_r}\int_0^{l_r} Z^4(X)dX\right]$	$Sp = \frac{1}{N}\sum_1^{N-1}\left\lvert\frac{Z(i+1) - Z(i)}{X(i+1) - X(i)}\right\rvert$

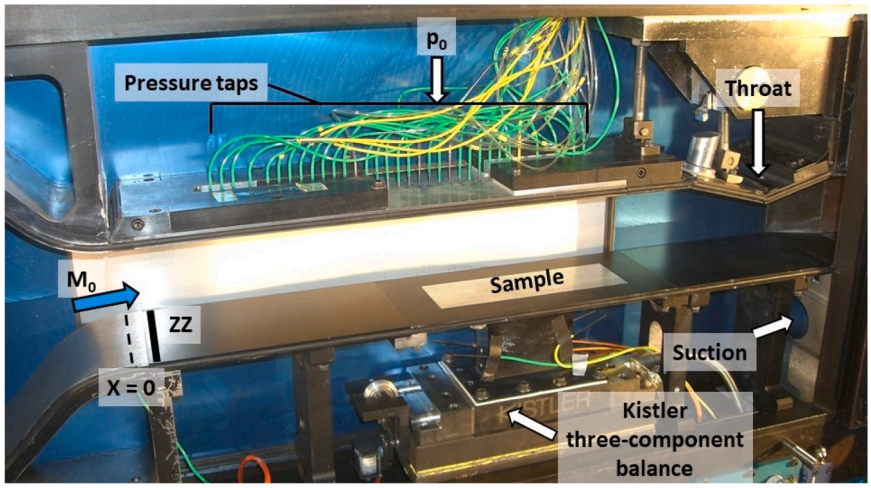

Fig. 1. Experimental set-up in the ONERA S8Ch wind tunnel [14].

roughness *Ra*, when evaluating the potential impact of surface roughness on drag. The roughness profiles and distributions of three of the samples studied in S8Ch are shown in Figs. 2 and 3. They were obtained using a Mitutoyo feeler device (evaluation length of 12.5 mm with one point every 1.5 μm). The so-called reference sample (RS) with a *Ra* value between 0.5 and 1 μm corresponds to the surface roughness of the CRM model tested in the S1MA wind tunnel, the pressure-sensitive paint (PSP) sample corresponds to paint covered with talc in one of the tests of the aforementioned second S1MA campaign, and the mirror-polished (MP) sample is given as a comparison point. Despite the theoretical limitations discussed in [14], concerning in particular the validity of the equivalent sand-grain height approach in the transitionally-rough and waviness regimes as evoked by Flack and Schultz [24], the RANS calculations were quite successful in reproducing the experimental positioning of the different sample drags.

The goal of the present work is to apply what has been learnt from the S8Ch study to refine the understanding of the initial observation made in the S1MA wind tunnel. More specifically, the study aims at assessing the effect of surface roughness on the lift and drag coefficients of transonic aircraft configurations, either in wind-tunnel or in flight conditions, and ultimately at proposing a way of taking it into account within applied aerodynamics computations in an engineering framework.

As a consequence, the article will be structured as follows. First, the S1MA and S2MA wind-tunnel facilities of ONERA (where tests with the same aircraft geometry have been carried out) will be presented, followed by a description of the CRM models, test conditions and correction methods. At a second step, the presentation will focus on the numerical simulation strategy (geometries and computational grids used for the calculations), as well as the RANS solver, its equivalent sand-grain height model, and the far-field drag breakdown methodology. The results will then be given for the S1MA experimental campaign alongside with several aspects such as turbulence model effects, roughness effects without and with Pressure-Sensitive Paint, and Mach number effects. In addition, a comparison will be performed between the surface roughness impacts in S1MA and S2MA. Results of numerical simulations will finally be presented at flight conditions for a full-scale aircraft in order to evaluate the effects and possible gains with respect to conditions in the wind-tunnel experiments, before presenting the main conclusions and perspectives of the study.

2. Wind tunnel tests

2.1. Wind tunnel facilities

The S1MA facility is a continuous atmospheric wind tunnel operating in the sub/transonic regime. It was put into service in 1952 and is equipped with two contra-rotating fans, driven by Pelton turbines moved by a waterfall with a total hydraulic power up to 88 MW. The wind velocity can be varied from a few meters per second to approximately Mach

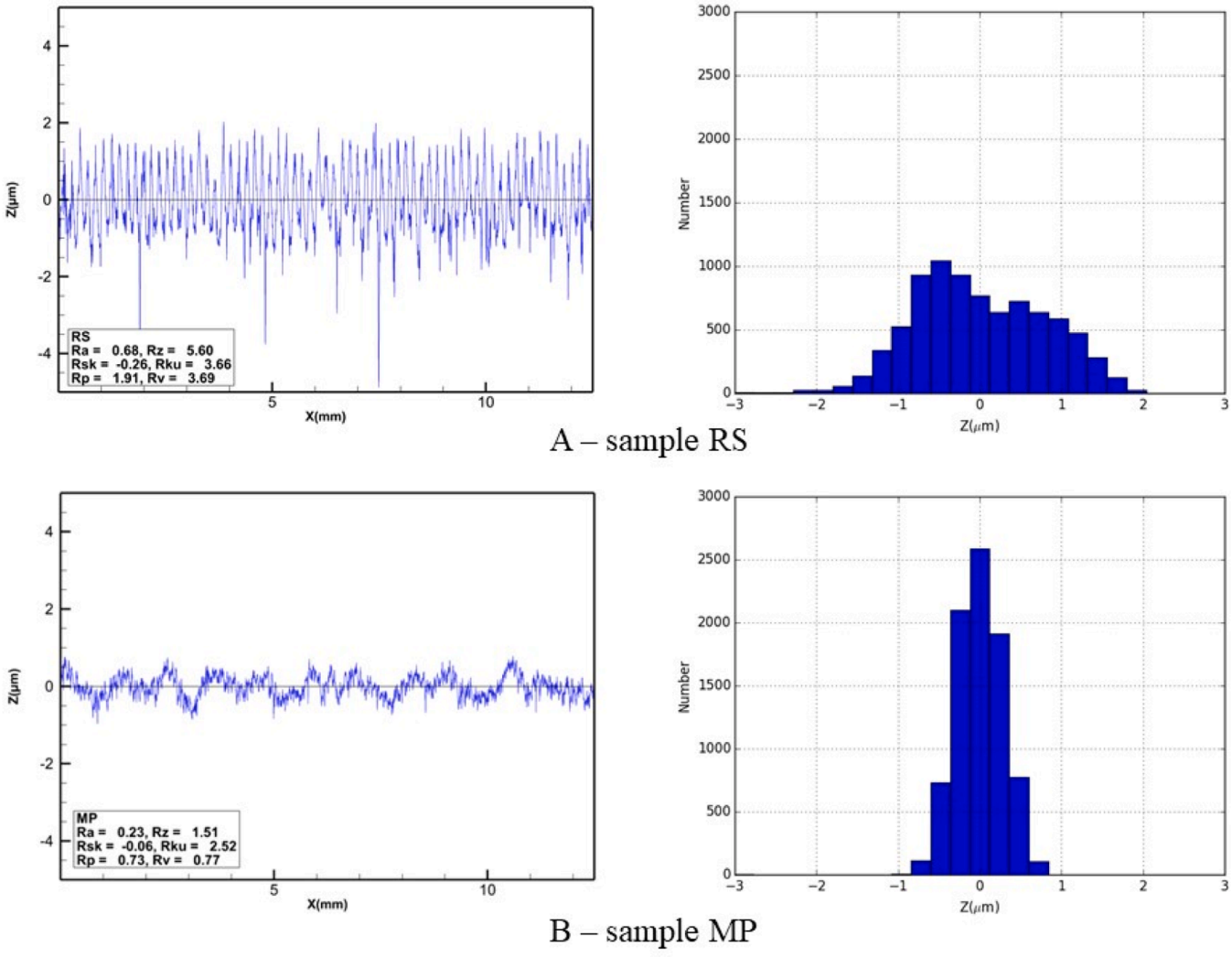

Fig. 2. Reference sample (A) and mirror-polished sample (B): roughness profiles (left), histograms of amplitude distributions (right) [14].

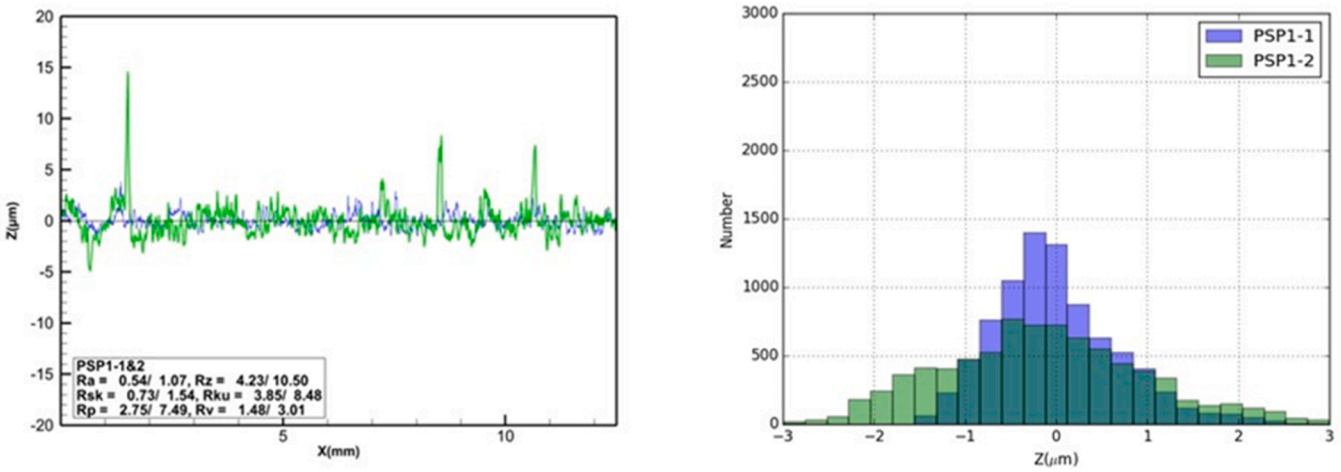

Fig. 3. PSP sample: PSP1–1 and PSP1–2 corresponding to two different measurement locations: roughness profiles (left), histograms of amplitude distributions (right) [14].

1 by varying the fan rotation speed. The total length of the aerodynamic circuit is about 400 m (see Fig. 4). The test section dimensions are 14 m in length and 8 m in diameter. For a Mach number around 0.85, the Reynolds number per meter is about 11 million.

A peculiarity of the circuit is the absence of heat exchanger. The temperature is controlled by letting outside fresh air enter the circuit. Hot air naturally exhausts around the edge of the contraction through an annular exit. An exhaust rate of about 10% of the total mass flow is required to maintain a temperature of about 50 °C in the tunnel.

The S2MA facility is a continuous wind tunnel operating in the subsonic, transonic and supersonic regimes. It was put into service in 1961. The air is driven by a 16-stage axial compressor powered directly by four Pelton turbines generating a power up to 55 MW. The total length of the aerodynamic circuit is about 100 m (see Fig. 5). It consists of two interchangeable rectangular test sections installed in a sealed enclosure. In this study, only the transonic test section has been used (1.75 m width x 1.77 m height). This test section has porous walls to limit the wall interference and avoid blockage. For a Mach number around 0.85, the Reynolds number per meter can go from approximately 3 to 26 million by varying the dynamic pressure (see Fig. 6). The temperature is controlled by a water exchanger in the aerodynamic circuit just downstream of the compressor.

2.2. CRM models

Before diving into the details concerning the models, some contextual information should be given concerning the interest of choosing the CRM geometry as a reference for such studies. Initiated in the early 2000s with the support of the American Institute of Aeronautics and Astronautics, the Drag Prediction Workshop (DPW) series is aimed at assessing the existing CFD methods used for civil aircraft aerodynamic performance prediction. For this purpose, the workshop's subsequent editions have involved different aircraft geometries which were computed by the workshop participants. The Common Research Model (CRM) emerged for the DPW-4 in 2009 and was still used up to the recent DPW-7 [25] in 2022. The configuration offers several advantages for research centres. Besides being a public geometry, it is representative of modern commercial transport aircraft with supercritical transonic wings (cruise Mach number of 0.85 with a corresponding lift coefficient $CL = 0.5$) and experimental tests with available databases have been carried out on it by different organisations (NASA, ETW, JAXA, ONERA) [26,27]. The Civil Aircraft Unit of ONERA took part in many of the previous DPWs [28–31] and also designed the CRM vertical tail geometry [32] used in the present study.

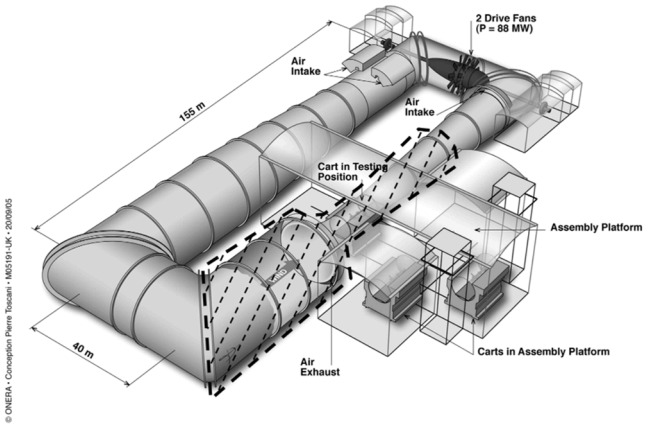

Fig. 4. S1MA air circuit.

The wind-tunnel model used in S1MA is called the ONERA Large Reference Model (LRM) and has the same geometry as the original CRM configuration. It was sized to 220% of the NASA model, the scale being 1/16.835 (full-scale dimensions are given in section III). The S1MA model is defined by a mean aerodynamic chord $Lref(\text{S1MA}) = 0.4161$ m, a reference surface area $Sref(\text{S1MA}) = 1.3538\ \text{m}^2$ and a span $b(\text{S1MA}) = 3.4905$ m. It was designed so that it has the same shape as the CRM model tested in the NASA NTF wind tunnel at the cruise point. The main dimensions of the model are given in Fig. 7, followed by a view of the test section showing the S1MA model on its support system (Z-sting setup) in Fig. 8. In addition, the roughness was measured with a Mitutoyo feeler device. On the surface of the wings and tails the average roughness *Ra* is between 0.4 and 0.5 µm, and on the fuselage surface *Ra* is around 0.5 µm.

The model used in the S2MA wind tunnel also has the same geometry as the original CRM. It was sized to 74% of the NASA model, the scale here being 1/50. As a consequence, the S2MA model is defined by mean aerodynamic chord $Lref(\text{S2MA}) = 0.1401$ m, reference surface area $Sref(\text{S2MA}) = 0.1535\ \text{m}^2$ and a span $b(\text{S2MA}) = 1.1753$ m. It was designed so that its shape for the highest dynamic pressure in S2MA matches that of the S1MA model at cruise point. The S2MA model with its Z-sting setup is shown in Fig. 9. Although the surface roughness is a bit better for this model (*Ra* values below 0.5 µm on the whole geometry), the same equivalent sand-grain roughness height will be considered for the computations presented in the following sections.

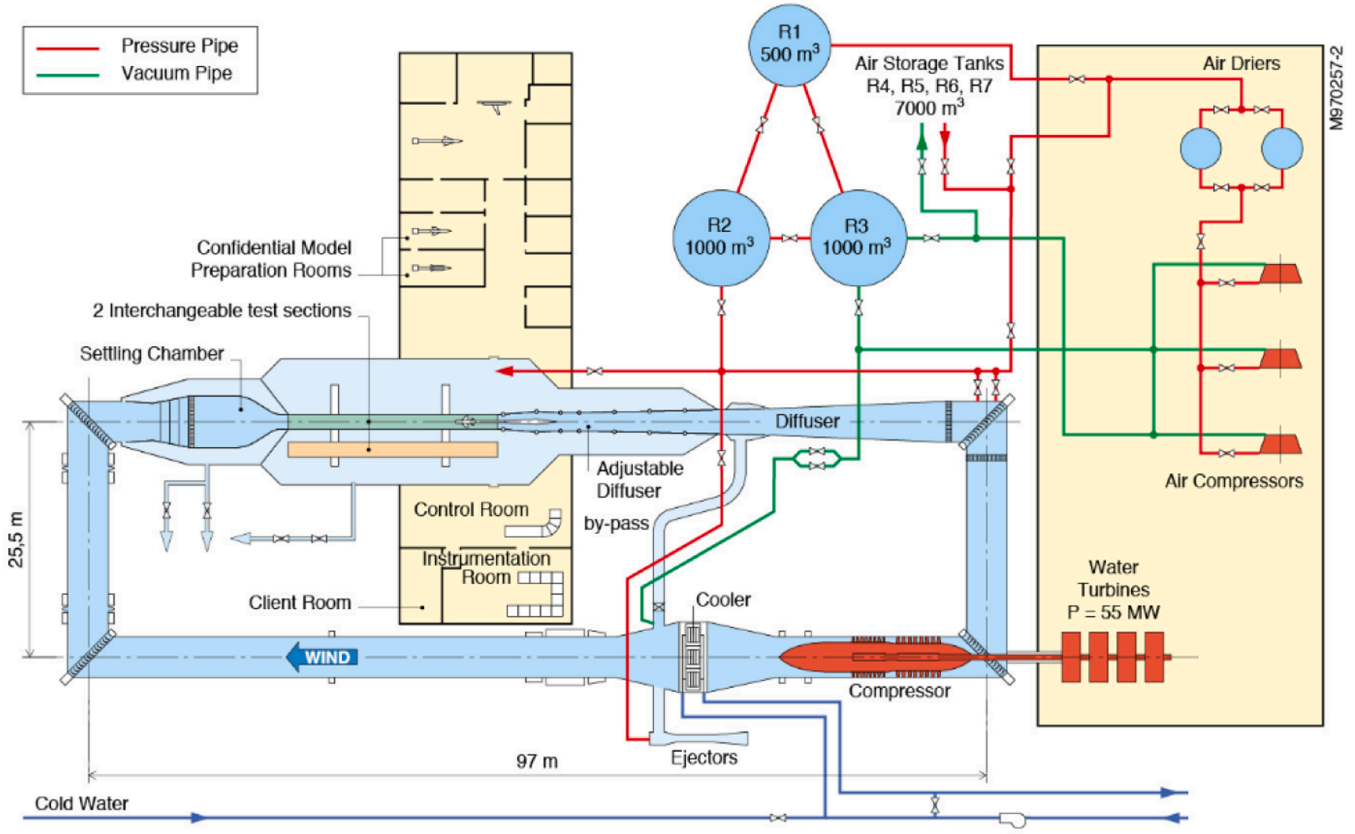

Fig. 5. S2MA air circuit.

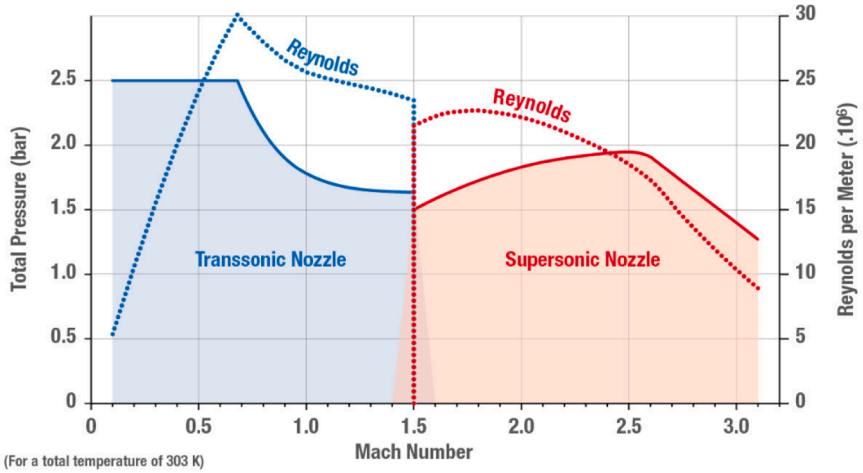

Fig. 6. S2MA operating range.

2.3. Measurements and test conditions

Pressure distributions for the S1MA model were measured on both the left and right wings using 270 pressure orifices located in nine spanwise stations (the same as the NASA CRM model): five on the right wing ($\eta = 0.131$, 0.283, 0.502, 0.727 and 0.950) and four on the left wing ($\eta = 0.201$, 0.397, 0.727 and 0.846). On the S2MA model they were measured on both wings using 64 pressure orifices located in four spanwise stations: two on the right wing ($\eta = 0.502$ and 0.727) and two on the left wing ($\eta = 0.201$ and 0.727). All pressure measurements were made using Electronically-Scanned Pressure (ESP) modules installed inside the forward portion of the fuselage.

As already mentioned above, tests with Pressure-Sensitive Paint were also performed during a second experimental campaign. One of the techniques involves layers of paint covered with talc (after 10% of the chord length), which might be better for the cameras as the light reflections are reduced. In this case, the PSP with talc was applied only on the model wings and the surface roughness characteristics were really similar to the ones of the PSP sample shown in Fig. 3.

In both wind tunnels, the tests were carried out in a Mach number range going from $Ma = 0.30$ up to $Ma = 0.95$. The Reynolds number based on the mean aerodynamic chord was 4.65 million in S1MA, and from 1.76 to 3.68 million in S2MA. The incidence range was from $-3.0°$ to $+10.0°$ depending on the test conditions. The incidence of the model

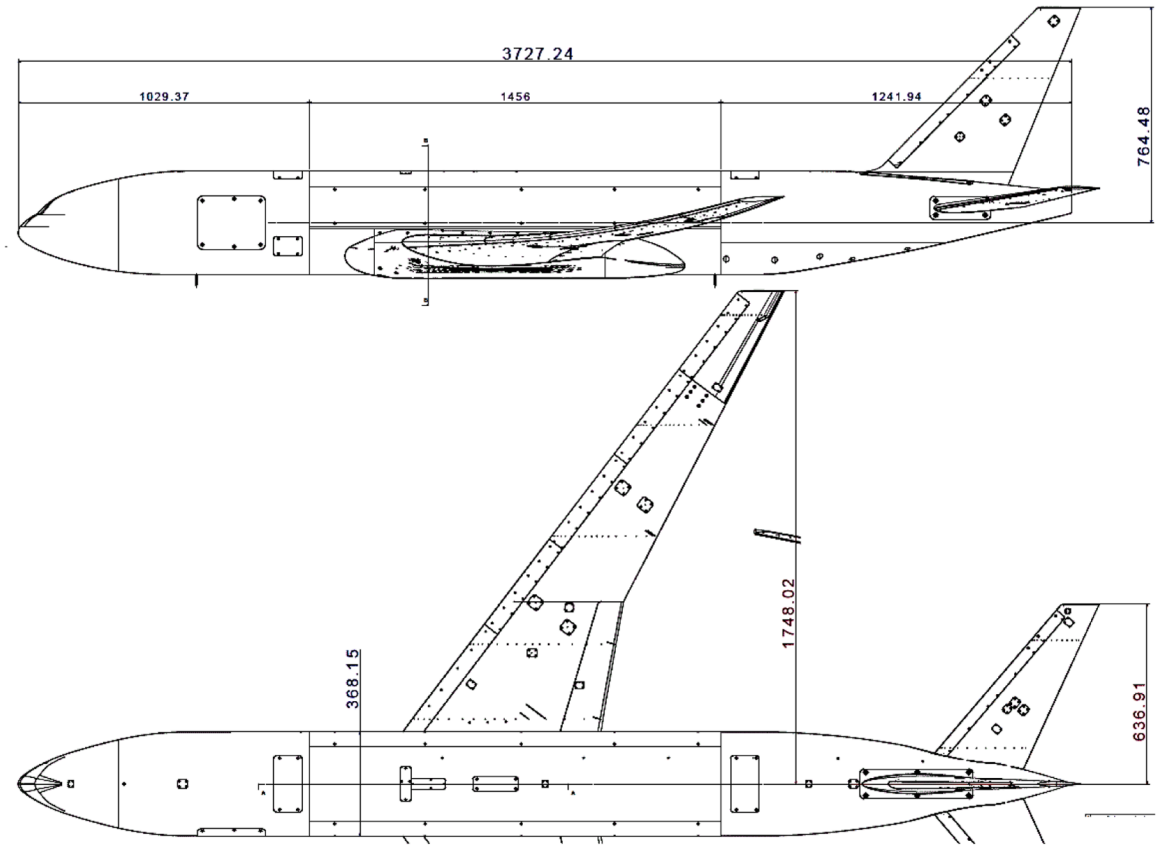

Fig. 7. Main dimensions of the CRM S1MA model (in millimeters).

Fig. 8. S1MA model with PSP on the wings in the wind tunnel test section.

was measured by means of three goniometers connected to the weighed balance adapter. It was corrected from wall and sting effects (as explained in the next section II.D), and the upwash was determined during the campaign. The forces and moments of the models were measured with a six-component balance equipped with two temperature sensors. In S1MA, wing deformation measurements were performed with two high-resolution cameras located behind a window in the ceiling of the test section [33]. The bending and twist deformations of the right wing were derived from the comparison of the 3D target positions between wind-on and wind-off conditions. The twist measurements obtained at $Ma = 0.85$ and $CL = 0.5$ were in good agreement with the data of the NASA and ETW wind-tunnel campaigns.

The transition of the boundary layer on the different parts of the models was forced by means of Cadcut strips. A Cadcut strip consists of an adhesive band on which dots (measuring 1.3 mm in diameter) are precut by laser at regular intervals (spaced 2.4 mm apart). As in the NASA tests, the trip dots were installed at 10% chord on the wings, the HTP and the VTP, and at a distance of 60 and 18 mm from the fuselage nose in S1MA and S2MA respectively. The characteristics are described in Table 2. Some acenaphtene visualizations were performed at the beginning of the test campaigns in order to verify the effectiveness of the boundary layer tripping.

2.4. Correction methods

The aerodynamic interferences are taken into account thanks to a correction process composed of several contributions:

1) The empty test section correction: it is a Mach number correction that results from a test section tunnel calibration.
2) The buoyancy correction: it is the effect of the empty wind tunnel Mach number gradient on drag (which is proportional to the product of the gradient and the effective volume of the body).
3) The wall effect correction: these corrections rely on the potential flow theory [34]. Under the assumption that the flow in the tunnel is irrotational outside the boundary layers and wakes, it can be described by a velocity potential $U_0 x + \varphi$. Assuming that the velocity perturbations $\partial x\varphi$, $\partial y\varphi$ and $\partial z\varphi$ are small with regard to U_∞, one comes to the well-known linearized potential equation:

$$\left(1 - Ma_\infty^2\right)\partial_x^2\phi + \partial_y^2\phi + \partial_z^2\phi = 0 \tag{1}$$

with boundary conditions at solid walls being linearized as well.

Unfortunately, this last assumption is less and less valid as the upstream Mach number Ma_∞ values approach $Ma = 1.00$ and as

Fig. 9. S2MA model in the wind tunnel test section.

Table 2
Cadcut trips used in the S1MA and S2MA tests (μm).

Trip heights	Wings	Tails	Fuselage
S1MA	142	127	152
S2MA	89 (inner wing) 78 elsewhere	78	78

typical transonic phenomena occur on the model, with large fluid accelerations up to supersonic regime.

This equation and the corresponding boundary conditions can be solved through a distribution of singularities on the model and support. The intensity of each singularity is based on the cross section areas, the lift and the drag.

Once the proper singularities have been set up, the linearity of Eq. (1) allows the potential φ to be broken down into a field φm generated by the model and a field φs generated by the support. Hence $\nabla\varphi m = (um, vm, wm)$ is the field of velocity distortion generated by the wall.

Once the velocity field ∇φm is known, a field of Mach number distortion can be determined:

$$\delta Ma = Ma_\infty \left(1 + \frac{\gamma - 1}{2} Ma_\infty^2\right) \frac{u_m}{U_\infty} \tag{2}$$

and a field of angle of attack distortion (upwash):

$$\delta Alpha = \frac{w_s}{U_\infty} \tag{3}$$

These fields are then averaged in space over areas of aerodynamic significance.

The Mach number correction ΔMa is taken as the value of δMa at ¼ of mean aerodynamic chord. The alpha correction is computed from a slightly more elaborated process: it is chord-averaged along the span, at ¾ of local chord, this correction enabling the lift correction to be zero (theory of Pistolesi [35]).

Second order corrections on drag (buoyancy correction due to velocity distortion) and pitching moment (mainly due to the HTP lift gradient to alpha) are then calculate

4) The sting corrections: these corrections are calculated thanks to RANS computations [36]. First order corrections are determined thanks to a pairing process. Simulations with and without support are considered as paired when the flow fields around the wing are similar. The criterion of similarity is the RMS of pressure coefficient distortion on the wing. The corrections applied to forces and moments are deduced from the differences between the integrated forces over the model with and without support.
5) The sting cavity pressure correction: this correction results from the presence of a non-zero pressure coefficient inside the rear fuselage which is "open" to enable sting entry. It consists in replacing the mean measured cavity pressure by the reference pressure on the cavity surface.

3. Numerical geometries and grids

3.1. CRM numerical geometries

The CAD files of the Common Research Model are available on the DPW website [3]. Different configurations of the CRM exist, some of them including a nacelle / pylon installation, but only the wing-body (WB) and wing-body with horizontal and vertical tails (WBHV) will be used in this study. Fig. 10 shows the WBHV configuration in full-scale dimensions as will be computed when dealing with the flight conditions. This geometry is defined by a mean aerodynamic chord $Lref = 7.00532$ m, a reference surface area $Sref = 191.8448$ m^2 (half configuration), a semi-span $b/2 = 29.38145$ m, an aspect ratio $AR = 9.0$, and a moment center at $Xref = 33.6776$ m, $Yref = 0.0$ m, and $Zref = 4.5203$ m.

The wing deformation is taken into account according to the angle of attack and the associated loading (twist and bending values) evolve along the polar. These deformations have been defined following the experimental database obtained in the European Transonic Wind tunnel

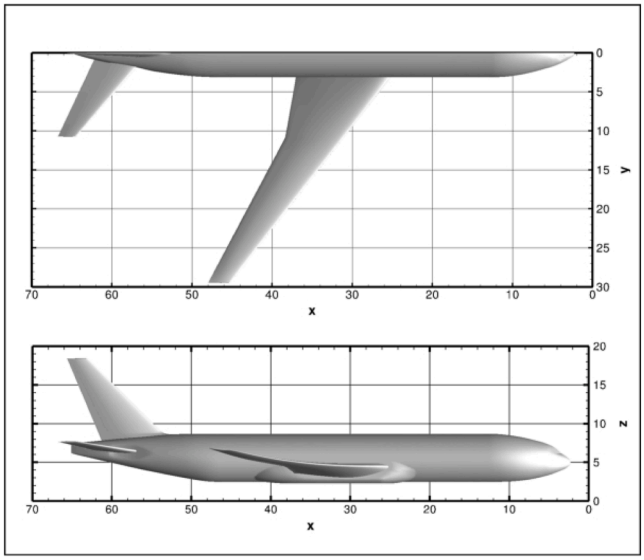

Fig. 10. CRM WBHV configuration at full-scale (in meters).

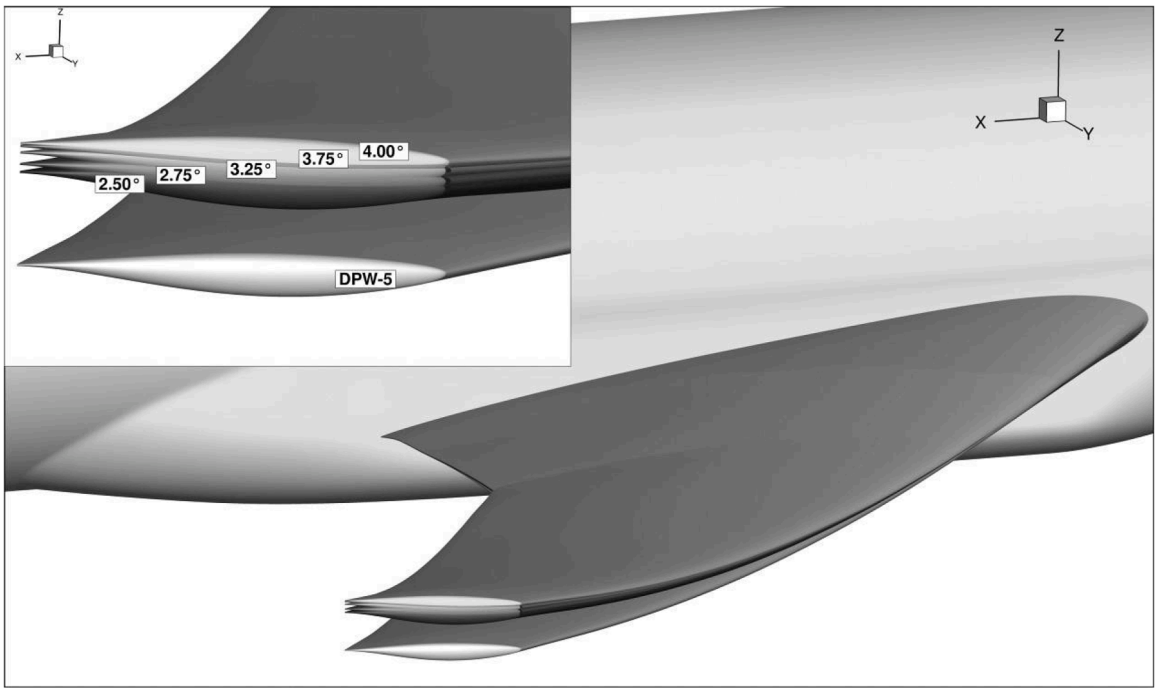

Fig. 11. Numerical wing shapes at different angles of attack.

(ETW) [27]. Fig. 11 illustrates the loading effect compared to the initial DPW-5 jig shape. In the present work, four different wing geometries have been used, corresponding to the angles of attack of 2.50, 2.75, 3.25, and 3.75 degrees. At the highest angles of attack, the loading produces more pronounced nose-down profile sections in the outboard wing. In addition, the twist variation, which was studied in [29], induces non-negligible effects on drag even though it is less visible than the bending change. For the computations of drag polars performed at angles of attack of 2.00 and 2.25 degrees, the 2.50-degree geometry will be used as the closest numerical shape available.

3.2. CRM overset and point-matched grids

The present study was based on high-quality computational grids for the WBHV and WB CRM configurations in order to ensure the accuracy of the RANS computations aimed at evaluating the roughness effect on aerodynamic forces. For the simulations in wind tunnel conditions and thus for the WBHV geometry, the grid family referred to as "overset_grids_Boeing_Serrano.REV00" [37] of the DPW-6 have been used. This family of structured overset grids was provided in 2016 by the DPW committee. In the present study, only the grids corresponding to the medium refinement level are considered. They are made of about 25 million points and the average normalized first cell size Y^+ is close to 0.5 for a Reynolds number of 5 million. The grid-convergence test case carried out in [30] showed that this medium level is fine enough for a drag prediction with accuracy below the drag count, one drag count (dc) being equal to 1×10^{-4}. As already evoked in the previous section, four different grids corresponding to the different loaded wing geometries will be computed (angle of attack of 2.50, 2.75, 3.25 and 3.75 degrees). These are O-type overset grids created by extrusion of the surface discretization (see Fig. 12) while the background computational domain is resolved by three Cartesian boxes of decreasing refinement levels. Each grid contains eight different bases (fuselage, wing, collar, horizontal tail, vertical tail, box_in, box_mid, box_out). Through this generation process, a precise control is achieved on the grid quality, such as grid spacing, stretching ratio and grid orthogonality near configuration surfaces. Moreover, several cell layers of the same height ensure an accurate gradient computation near the aircraft skin surface. The grid extent is

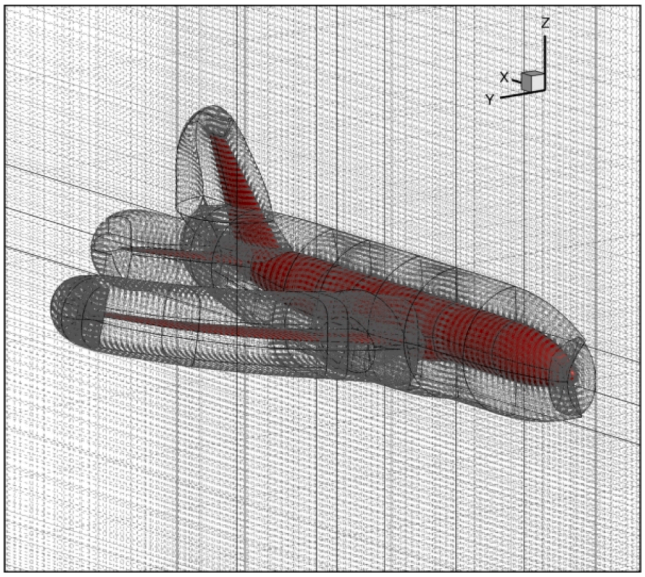

Fig. 12. Illustration of the overset grid topology (WBHV).

greater than 500 mean-aerodynamic chords. Before running these overset grids of Boeing with the elsA solver, a necessary pre-processing step has been performed. Along the whole process, the in-house Cassiopée library [38] has been extensively used, especially in order to build the blanking variable field (defining whether a grid cell is blanked, computed or interpolated).

Unfortunately, the grids that have just been presented are not suitable for computations in flight conditions, at greater Reynolds numbers. It was therefore decided to perform these computations using some grids of the CRM WB configuration provided in the frame of DPW-7 [25]. This version of the workshop was aimed at "expanding the envelope", thus including grids generated for Reynolds numbers up to 30 million, with first cell heights much smaller than in the previous workshops. The chosen grids are the point-matched structured family of grids referred to

as "Vassberg_Grids.REV00" [39]. They are built on a half configuration with an O-type topology composed of 5 structured blocks (i, j, k), as illustrated in Fig. 13 showing a plane Index(i) = constant on the suction side as well as the symmetry plane. They have at least two constantly-spaced cells at viscous walls. The growth rates do not exceed 1.2, the wing spanwise spacing is below 0.1% of the semi-span at root and tip, and the chordwise spacing is under 0.1% of the local chord length at leading and trailing edges, the trailing edge itself being discretized by at least 8 cells. The farfield boundary is located at more than 100 semi-span lengths. The medium refinement level employed here is composed of about 42 million points and, as with the overset grid family, four different grids are available according to the angles of attack considered. Moreover, these are the DPW-7 grids aimed at the low dynamic pressure conditions (LoQ) as they are expected to be more suitable for the high-altitude conditions.

4. CFD solver and far-field post-processing

4.1. elsA solver

The RANS computations presented here have been performed with the elsA solver (ONERA and Safran property) [40]. This software uses a cell-centered finite-volume discretization on structured point-matched and overset grids. The time integration is carried out by a backward-Euler scheme with implicit LU-SSOR relaxation. The spatial discretization is realized using a 2nd order centered scheme with Jameson-like artificial dissipation [41]. Multigrid techniques with one coarse grid level were used to accelerate convergence to the steady-state solution. The computations are either fully turbulent or integrate the 10% chord laminar zone existing in the experiments. Turbulence effects are simulated by the one-equation Spalart-Allmaras (SA) model [42] and mostly by the k-ω Shear Stress Transport (SST) model of Menter [5]. Both models have been complemented by the Quadratic Constitutive Relation (QCR-2000) [43], a nonlinear closure which is not based on the traditional Boussinesq relation.

In order to reach a satisfactory level of convergence, the computations were continued until the forces were stable enough to observe a lift coefficient variation lower than +/- 0.001 and a drag coefficient variation lower than one drag count over the last thousand iterations. For instance, Fig. 14 shows the aerodynamic force convergence over 8000 solver iterations for the WBHV configuration run on the overset grids in the S1MA conditions, with and without accounting for surface roughness in the computation. As expected from previous studies using similar numerical methods, the friction drag *CDf* is the one exhibiting the fastest convergence. It can also be observed that taking the surface roughness into account in the solver does not impact the convergence behaviour. The same was observed for the WB point-matched grids. Some of the effects of surface roughness on the aircraft performance that will be studied in the article are already apparent in the results shown in Fig. 14. Finally, the numerical simulations with the elsA solver were carried out using 48 to 196 CPU cores in an in-house cluster.

4.2. The equivalent sand-grain roughness height method

Besides the general settings presented above, a method based on the equivalent sand-grain height was used in the solver to model the surface roughness effects. This equivalent height corresponds to the virtual size of the uniformly packed sand grains tested by Nikuradse [15] that would produce the same frictional drag as the considered surface in the fully-rough regime. Three models based on this approach are available in the elsA solver. The one named AGC [11], for Aupoix-Grigson-Colebrook, was chosen for the present study, in combination with the k-ω SST model, as it was the case in the S8Ch study (see Introduction).

With the equivalent sand-grain height method, the only user-provided input to the solver's roughness model for a given surface is the k_s value. Jiménez [18] has deemed the notation $k_{s\infty}$ more appropriate, referring to the fact that this variable, which is in turn used to calculate the roughness Reynolds number $k_s^+ = (U_\tau/\nu)^* k_s$ (with U_τ being the friction velocity and ν the kinematic viscosity), is a property of the surface normally valid only in the fully-rough regime. Similarly to the S8Ch wind-tunnel experiment [14], the computations of the present study will mostly take place in the transitionally-rough regime (intermediate between the hydrodynamically-smooth and the fully-rough regimes, corresponding to the regime where the friction is equivalent or even dominates the pressure forces). The idea here is to apply the pragmatic approach already used for the S8Ch study, since its outcomes were found to be satisfactory. To avoid confusion, the notation k_{sTrans} will be adopted when necessary in the rest of this work.

As explained in the Introduction, the surface samples RS and PSP tested in S8Ch correspond to the model surfaces and paint that will be analyzed in this work. More precisely, RS has a surface finish really close to the one of the S1MA model but might be slightly too rough compared to that of the S2MA one. The k_s values that can be used for both in the numerical computations are extracted from [14], where they were calculated with the Mucker-type correlation involving the *Rq, Sk, Ku* and *Sp* roughness parameters. The correlation of Schäffler $k_s = 8.9Ra$ [44] proposed for forged and machined blades in 1980 will also be used as a

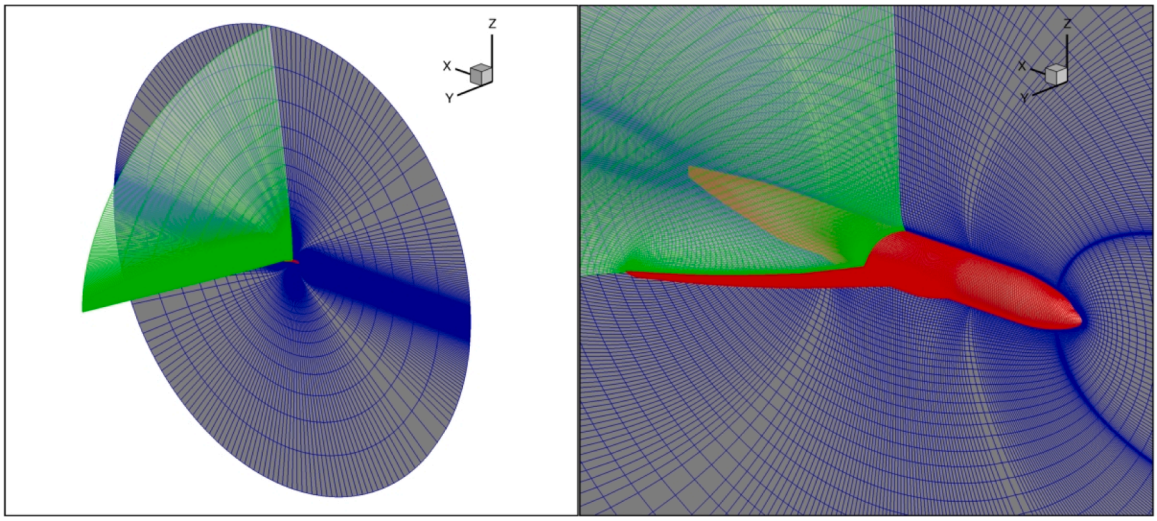

Fig. 13. Illustration of the point-matched grid topology (WB).

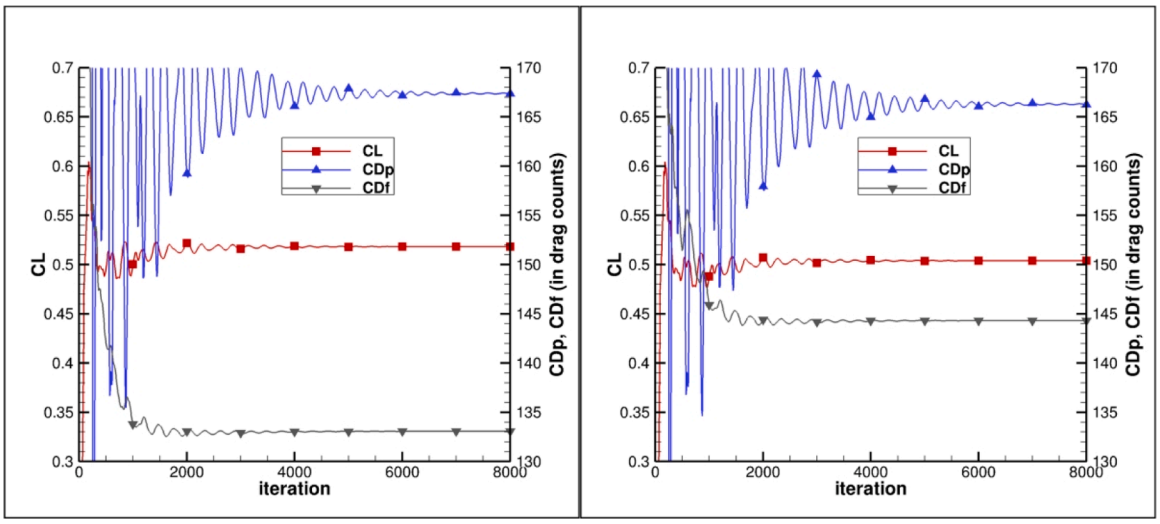

Fig. 14. Force convergences; WBHV without (left) and with roughness (right); overset grids; S1MA conditions; $Ma = 0.85$, $Re = 4.65\times10^6$, $alpha = 2.75°$.

Table 3
k_{sTrans} values for the different surfaces (μm).

Correlation	Mirror-Polished (MP)	Reference Sample (RS)	PSP1 average
Musker-type [14]	1.9	6.6	15.0
Schaffler [44]	2.0	6.1	7.2

comparison / reference. Table 3 gives the different values, from which one may observe that both correlations produce very similar results for the bare metallic surfaces (MP and RS). A uniform value of 7 μm will be selected for the equivalent sand-grain height in the computations of the wind-tunnel models in S1MA and S2MA. However, for the painted surface PSP1 (for which an average of the parameters obtained at different locations is considered, see Fig. 3), the correlation based solely on Ra does not take enough parameters into account to give a relevant k_s value, as demonstrated in [14]. In this case, a uniform value of 15 μm will be selected, originating from the Musker-type correlation.

4.3. Far-field drag analysis

The standard and most straightforward method to compute aerodynamic performance coefficients consists in integrating forces on the aircraft skin, referred to as the near-field approach. This allows a mechanical breakdown of drag into its pressure and friction components. On the other hand, far-field methods are based on the evaluation of the effect of the aircraft on the fluid through a momentum balance. The formulations and methods relative to the far-field theory for drag calculation used in this work are presented in [45–47]. In the present study, all the far-field analyses are carried out with the drag extraction code FFDπ [31,48], coupled with the ONERA Cassiopée library [38].

The far-field drag approach aims at providing a physical drag breakdown into viscous, wave, and lift-induced drag components. In addition, this analysis can isolate an important part of the spurious drag, related to numerical approximation errors (e.g. dissipation and grid quality). In practice, it is carried out at the end of the CFD process, as a post-processing tool working on the numerical solutions provided by the solver.

The different drag coefficients which are used in this article are defined below. The near-field drag is defined as the sum of pressure and friction drags:

$$CDnf = CDp + CDf \tag{4}$$

The far-field drag is defined as the sum of the viscous, wave and induced drag components:

$$CDff = CDv + CDw + CDi \tag{5}$$

$$CDsp = CDnf - CDff \tag{6}$$

The spurious drag $CDsp$ corresponds to drag generated through entropy or stagnation enthalpy variations along streamlines outside physical viscous layers and shocks, and not resulting from vortex decay. It is mainly produced in regions of strong pressure gradients via the addition of artificial dissipation in the numerical flux. The viscous pressure drag $CDvp$ is the part of the viscous drag which is not directly associated to the friction drag (boundary layer displacement or wake effects, flow separation):

$$CDv = CDvp + CDf \tag{7}$$

The far-field formulation allows for the following near-field/far-field drag balance:

$$CDp + CDf = CDv + CDw + CDi + CDsp \tag{8}$$

Fig. 15. Far-field integration volumes for $CDvp$ (grey) and CDw (black); WBHV without surface roughness; overset grids; S1MA conditions; $Ma = 0.85$, $Re = 4.65\times10^6$, $alpha = 2.50°$.

Fig. 15 shows the far-field integration volumes for the viscous pressure and wave drag components on the WBHV geometry without surface roughness in the S1MA conditions. These volumes can allow interesting modifications of the shock or wake features to be highlighted, which might be useful in design and optimization processes.

5. Comparisons in S1MA conditions

In this section, the main objective is to compare the experimental results from the S1MA wind tunnel to the numerical data obtained with the elsA solver. The focus is clearly on lift and drag prediction with a particular emphasis on the *CL*(*CD*) polars. The roughness effects will be taken into account in the computations with the equivalent sand-grain height approach presented in the previous sections. The configuration is the WBHV CRM discretized by the overset family of grids and dimensioned in accordance with the S1MA model (scale 1/16.835). The aerodynamic conditions are the following: Mach number $Ma = 0.85$ (with the exception of the Mach number effect paragraph), stagnation pressure and temperature $P_i = 89{,}000$ Pa, $T_i = 323$ K, and Reynolds number based on *Lref(S1MA)* close to five million ($Re/\text{m} \sim 11\times10^6$).

5.1. Turbulence model effects

At this step the surface roughness is not considered in the computations at a first step, the aim of this paragraph being a first comparison of two turbulence models which are largely used in the aerodynamic design community. The computations without surface roughness are referred as "no-roughness" computations (NR). Six simulations are carried out for each model at a given angle of attack *alpha* ranging from 2.00 to 3.75 degrees using the appropriate wing geometry for each value as explained above. The near-field coefficients *CL, CD, CDp, CDf*, and *CM* obtained with the SA and k-ω SST models are given respectively in Table 4 and Table 5 (drag coefficients are in drag counts). It can be seen that for the latter an additional angle of attack is included in order to obtain a computation at $CL = 0.5$ (2.75° geometry), which will be used for further comparisons in the following. Fig. 16 shows the drag polars *CL*(*CD*) for both turbulence models. The experimental data obtained in the S1MA wind tunnel are also shown as a reference (corrected for wall and support system effects, as detailed in Sec. 2.4).

Before focusing on the drag polar curves, the tabulated results show that the SA and k-ω SST models have a very different *CL*(*alpha*) behavior. For example, there exists a substantial difference between the lift coefficient prediction for the two models at 2.50°, using the same geometry and grid, the computation with the SA model giving a lift coefficient of 0.4951 and the one with k-ω SST giving a value of 0.4833. This is also depicted in the relative position of the SA and k-ω SST points on the polars of Fig. 16. Furthermore, the friction drag is different between the SA and the k-ω SST model at 2.50°, which give $CDf = 136.8$ *dc* and 133.7 *dc* respectively. This difference of about 3 drag counts is quite constant along the polar.

When comparing the *CL*(*CD*) curves, it appears that the agreement is rather good between the two models up to $CL \sim 0.52$, but the SA model seems to underestimate the drag for greater lift coefficient values. At $CL = 0.6$, it gives values about 25 to 30 counts lower than the k-ω SST model or the experiments (both models are used with the QCR-2000 relation).

Table 4
SA model; NR; near-field coefficients; WBHV; S1MA conditions; $Ma = 0.85$, $Re(Lref(\text{S1MA})) = 4.65\times10^6$.

alpha (°)	*CL*	*CD*	*CDp*	*CDf*	*CM*
2.00	0.4185	251.4	113.6	137.8	−0.0500
2.25	0.4566	265.8	128.4	137.4	−0.0606
2.50	0.4951	284.5	147.7	136.8	−0.0715
2.75	0.5307	306.1	169.9	136.2	−0.0808
3.25	0.5936	362.3	227.8	134.5	−0.0937
3.75	0.6321	435.3	302.5	132.8	−0.08644

Table 5
k-ω SST model; NR; near-field coefficients; WBHV; S1MA conditions; $Ma = 0.85$, $Re(Lref(\text{S1MA})) = 4.65\times10^6$.

alpha (°)	*CL*	*CD*	*CDp*	*CDf*	*CM*
2.00	0.4074	246.9	112.4	134.5	−0.0475
2.25	0.4451	261.2	127	134.2	−0.0576
2.50	0.4833	279.1	145.5	133.7	−0.0681
2.62	0.500	288.3	154.9	133.4	−0.0713
2.75	0.5182	300.5	167.4	133.1	−0.0766
3.25	0.5771	355.1	223.6	131.6	−0.0860
3.75	0.6139	423.8	294.0	129.8	−0.0787

This was already observed in DPW-7 studies with different grids [31].

Another aspect of these results, corresponding to the initial observation mentioned in the Introduction, is the significant difference between the numerical and experimental drag polars. In particular, close to the design point at $CL = 0.5$, which is crucial in the aircraft performance prediction, these polars exhibit a difference of about 10 drag counts. Although representing only 3% of the total drag, this discrepancy it is far from being negligible in the frame of accurate comparisons between CFD and wind tunnel experiments.

5.2. Model roughness effects

In this paragraph, the surface roughness of the wind tunnel model is integrated in the solver computation. As explained in Sec. 4.2, an equivalent sand-grain height of 7 μm is used for this metallic surface finish whose *Ra* is around 0.5 μm. The near-field coefficients are given in Table 6 for the fully-turbulent rough-surface simulations and in Table 7 for the rough-surface computations considering laminar flow up to 10% chord on the wing (see Sec. 2.3). Taking into account the boundary layer tripping as well as the roughness effects is aimed at an improved representation of the experimental campaign. These tables are to be compared to Table 5.

First, it can be observed that the lift coefficient at iso-*alpha* is significantly reduced when considering the surface roughness. Indeed, the smooth computation at 2.50° gives $CL = 0.4833$ (cf. Table 5) whereas the rough-surface one gives 0.4695 (about 3% drop). On the contrary, the consideration of laminar flow at the wing leading edge produces, as expected, greater lift levels ($CL = 0.4799$ at 2.50°) which are intermediate between the smooth-surface and rough-surface fully-turbulent simulations. The effect of surface roughness on the pitching moment coefficient is a production of a lower nose-down value. For instance, the infinitely-smooth computation predicts $CM = -0.0681$ and the rough-surface one −0.0608 at $alpha = 2.50°$ Again, considering laminar flow up to 10% of the wing chord seems to counter this effect and gives a *CM* value of −0.0666, which is closer to the smooth-surface case.

Fig. 17 illustrates the figures of the *CL* and *CD* columns, in the form of the drag polars of the smooth-surface k-ω SST computations, the S1MA experimental data (as in Fig. 16) as well as the curves of the rough-surface simulations including the one considering laminar flow at the wing leading edge. This figure highlights the fact that laminar flow (boundary layer tripping) and surface roughness both have a significant impact on the aerodynamic coefficients. In particular, the effect of the surface roughness of the wind-tunnel model on the drag polar is substantial. The difference between the NR (smooth surface) and AGC 7 μm (rough surface) curves is 15–20 drag counts, i.e. +6–7%, for lift coefficients up to 0.5 and reaches about 30 dc at $CL = 0.6$. As a consequence, the drag underestimation of the numerical polar compared to the wind-tunnel data becomes an overestimation when surface roughness is considered in the numerical computations. Moreover, once laminar flow is imposed on the wing up to 10% chord, in addition to the consideration of surface roughness, the computations produce the expected effect of reducing the drag and give a very satisfactory agreement between the elsA and S1MA polars (see Fig. 17). This agreement is less

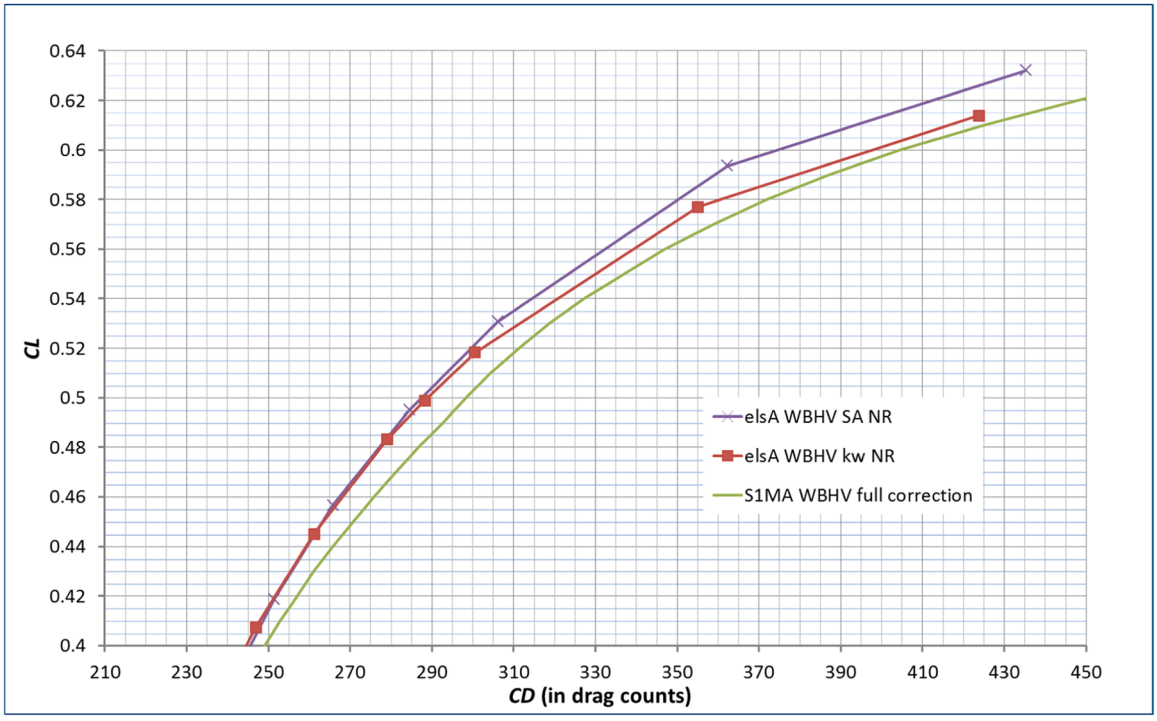

Fig. 16. Turbulence model effects; drag polars; WBHV; S1MA conditions; $Ma = 0.85$, $Re(Lref(\text{S1MA})) = 4.65\times10^6$.

Table 6
k-ω SST; AGC 7 μm; near-field coefficients; WBHV; S1MA conditions; $Ma = 0.85$, $Re(Lref(\text{S1MA})) = 4.65\times10^6$.

alpha (°)	*CL*	*CD*	*CDp*	*CDf*	*CM*
2.00	0.3948	259.5	113.6	146.0	−0.0412
2.25	0.4318	273.5	127.9	145.5	−0.0509
2.50	0.4695	290.4	145.4	145.0	−0.0608
2.722	0.500	308.0	163.6	144.4	−0.0677
2.75	0.5039	310.6	166.3	144.3	−0.0688
3.25	0.5627	363.3	220.7	142.6	−0.0781
3.75	0.6005	430.3	289.6	140.8	−0.0719

Table 7
k-ω SST; AGC 7 μm with laminar flow up to 10% chord; near-field coefficients; WBHV; S1MA conditions; $Ma = 0.85$, $Re(Lref(\text{S1MA})) = 4.65\times10^6$.

alpha (°)	*CL*	*CD*	*CDp*	*CDf*	*CM*
2.00	0.4034	255.9	113.6	142.3	−0.0461
2.25	0.4413	269.8	127.8	141.9	−0.0561
2.50	0.4799	287.2	145.7	141.4	−0.0666
2.641	0.500	298.0	156.9	141.1	−0.0708
2.75	0.5155	308.1	167.3	140.8	−0.0753
3.25	0.5761	362.3	223.1	139.1	−0.0859
3.75	0.6141	430.6	293.4	137.3	−0.0795

satisfactory at the lowest *CL* values, which might be due to the numerical geometry not being sufficiently representative of the wind-tunnel model shape for angles of attack below 2.50° (see discussion in Sec. 3.1). The main conclusion of the present comparison is not however the agreement between the numerical and experimental drag polars in this particular case, but rather that the effect of surface roughness should be considered in CFD computations aiming at investigating comparisons with experiments or at performing accurate pre-testing studies.

To further analyze the physical mechanisms due to the surface roughness effects, Table 8 shows some comparisons at iso-*CL* = 0.5 involving both the near-field and far-field drag coefficients. The percentages of contribution of the different components (see Sec. 4.3) are also given for the following cases: NR, AGC 7 μm, and AGC 7 μm with laminar flow up to 10% wing chord. It can overall be observed that in these wind-tunnel conditions the friction drag is responsible for 46–47% of the total aircraft drag (*CDff*), the viscous pressure drag *CDvp* represents 19–20%, the wave drag only 2–3%, and the lift-induced drag 30–32%. The negative effect of surface roughness is especially visible on the *CDi* percentage, which from 32.2% in the smooth-surface case is reduced to 30.5% in the AGC 7 μm computation, indicating that a significantly lower part of the total drag is dedicated to the lift production. Finally, it should be noted that the magnitude of the spurious drag component is low for these cases (below 0.25 *dc*) due to the quality of the DPW grids.

The two "Delta" lines for each individual coefficient of Table 8 give the difference in drag counts between each considered rough-surface case and the NR computation. As seen in Fig. 17, the fully-turbulent rough-surface simulation produces a total drag about 20 counts higher than the one of the smooth case at $CL = 0.5$. This difference of +19.7 drag counts at the same lift is composed of 11 dc of friction drag (56%), 6.5 dc of viscous pressure drag (33%), 1.2 dc of wave drag (6%), and 1.0 dc of lift-induced drag (5%). The evolution of the friction component is therefore found to be the leading mechanism responsible for the drag increase due to surface roughness, with the viscous pressure drag also representing a third of this increase. The friction drag difference of about 11 counts between the rough-surface computation and the NR one is almost constant along the whole polar. The same table shows that the total drag difference with respect to the NR case is reduced to about 10 counts (79% due to friction drag) for the rough-surface computation considering laminar flow at the wing leading edge region.

This study of integral coefficients can then be continued in terms of local analyses. First, to illustrate the impact of surface roughness on the friction drag, Fig. 18 compares the local friction coefficients extracted from elsA on a wing section at mid-span (50.2%) for the smooth-surface and rough-surface cases. On the left side, both computations are carried out at the same angle of attack, whereas on the right side they are carried out at the same lift coefficient. For the wing pressure side (part of the curves without the formation of a shock wave), the behavior in iso-*alpha* and iso-*CL* conditions is quite identical, corresponding to a significantly

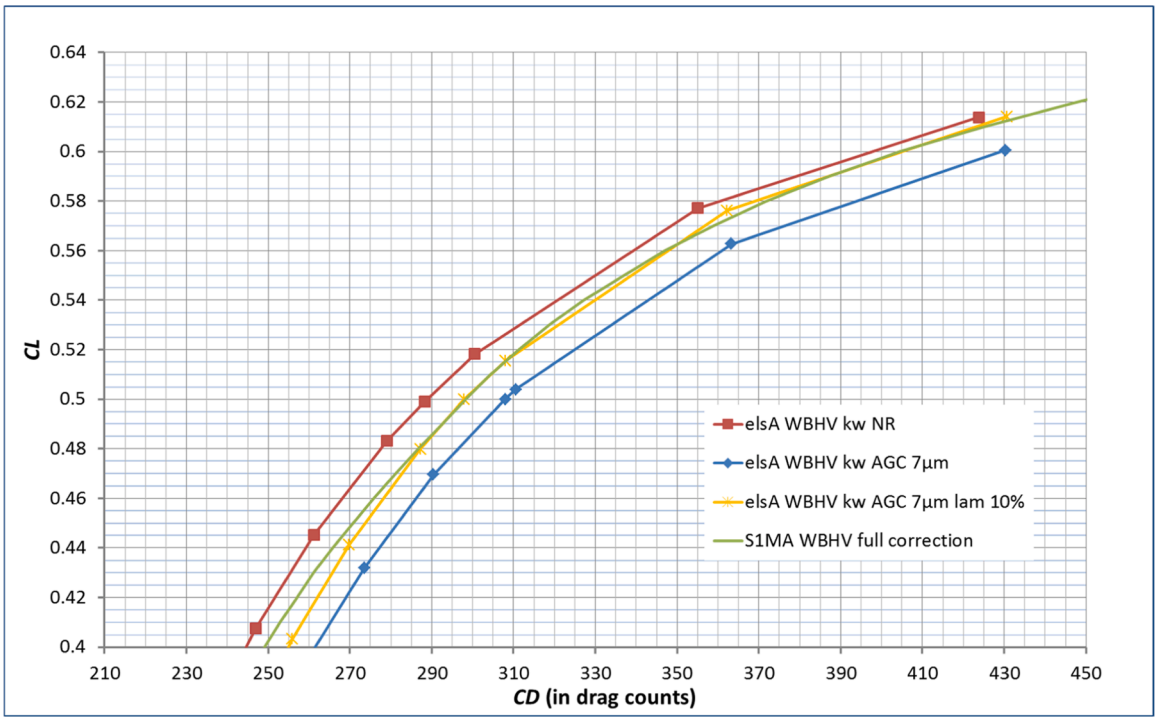

Fig. 17. Model surface roughness effects; drag polars; WBHV; S1MA conditions; $Ma = 0.85$, $Re(Lref(\text{S1MA})) = 4.65\times10^6$.

Table 8
k-ω SST; NR versus AGC 7 µm and AGC 7 µm with laminar flow; near and far-field coefficients; WBHV; S1MA conditions; $Ma = 0.85$, $Re(Lref(\text{S1MA})) = 4.65\times10^6$, $CL = 0.5$.

	CDp	*CDf*	*CDvp*	*CDv*	*CDw*	*CDi*	*CDff*
WBHV S1MA NR	154.9	133.4	54.4	187.8	7.8	92.9	288.6
% of *CDff*	53.7	46.2	18.8	65.1	2.7	32.2	100.0
WBHV S1MA AGC 7 µm	163.6	144.4	60.9	205.3	9.0	93.9	308.3
% of *CDff*	53.1	46.8	19.8	66.6	2.9	30.5	100.0
Delta AGC 7 µm - NR	8.7	11.0	6.5	17.5	1.2	1.0	19.7
WBHV S1MA AGC 7 µm laminar	156.9	141.1	56.3	197.4	7.6	93.3	298.4
% of *CDff*	52.6	47.3	18.9	66.2	2.5	31.3	100.0
Delta AGC 7 µm laminar - NR	2.0	7.7	1.9	9.6	−0.2	0.4	9.8

stronger *Cf* for the rough-surface case all along the chord but with a decreasing difference from leading edge to trailing edge. For the suction side, the curves at iso-*alpha* conditions exhibit a behavior similar to the pressure side except in the shock area, but in iso-*CL* conditions the friction penalty due to roughness is located upstream of the shock wave.

In order to understand the impact of surface roughness on the lift coefficient (see Tables 5 and 6), Figs. 19 and 20 show the pressure distributions for the NR and AGC 7 µm (with and without laminar flow)

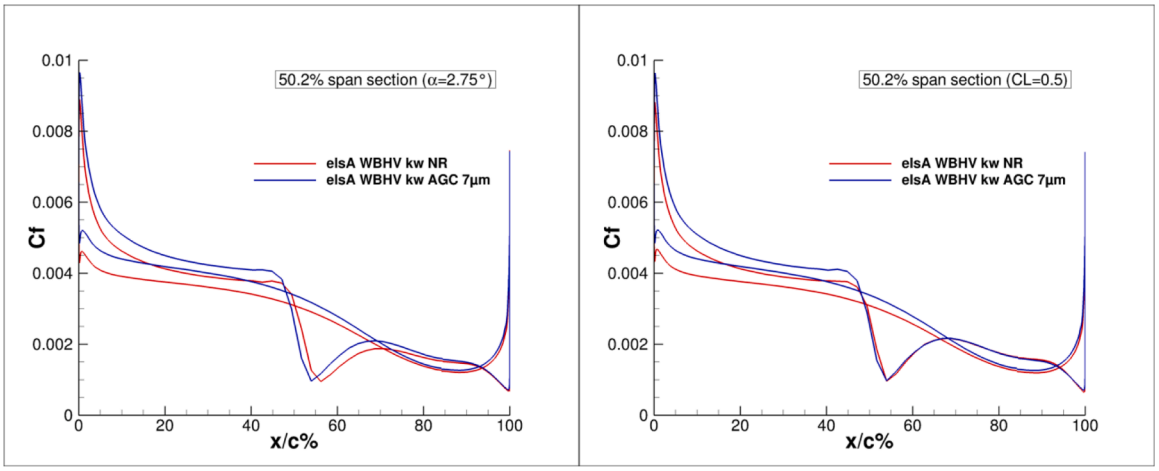

Fig. 18. *Cf* coefficient on wing section $\eta = 50.2\%$; WBHV; S1MA conditions; $Ma = 0.85$, $Re(Lref(\text{S1MA})) = 4.65\times10^6$, iso-*alpha* $= 2.75^\circ$ (left) and iso-*CL* $= 0.5$ (right).

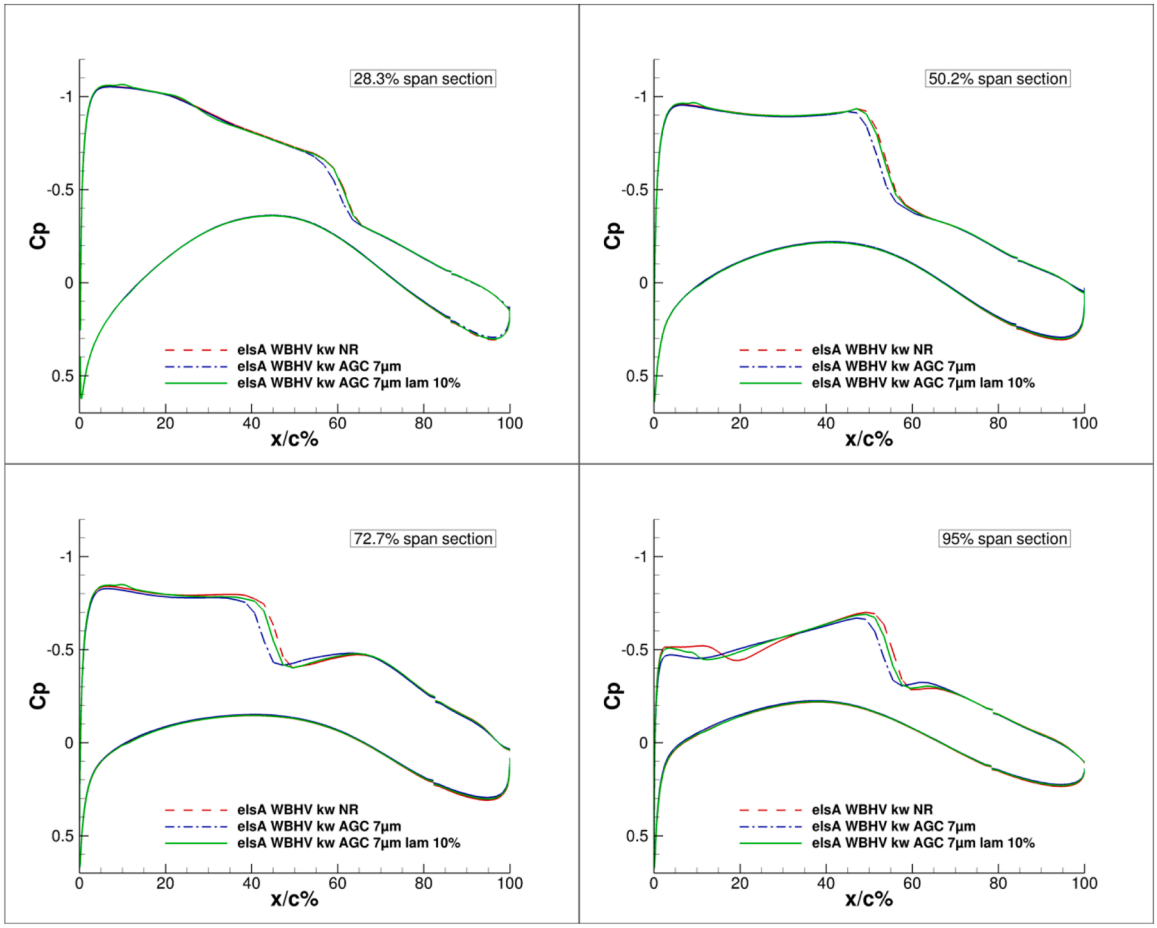

Fig. 19. *Cp* distributions on different wing sections; WBHV; S1MA conditions; $Ma = 0.85$, $Re(Lref(\text{S1MA})) = 4.65\times10^6$, iso-*alpha* = 2.75°.

computations at the 28.3%, 50.2%, 72.7%, 95% spanwise wing sections. The simulations are all carried out with an angle of attack of 2.75°. The results of Fig. 19 show that the surface roughness does not have a very large impact on the pressure distribution at the first three sections. The largest differences occur in the vicinity of the shock wave, which is a region of prime interest in transonic flows, and become more significant when moving towards the external part of the wing. Moreover, at 95% span, differences become significant also on the first 35% of the chord on the suction side. Fig. 20 then shows a detail of some key areas of the 50.2% section and explains why the computation using the surface roughness model produces less lift than the smooth-surface one. On the suction side, form the leading edge to the shock wave position, the fully-turbulent AGC 7 µm computation shows a lower negative pressure which induces a lift loss. In addition, the surface roughness also leads to a lift coefficient reduction on the pressure side, albeit less visible than on the suction side. The detail at the trailing edge region is consistent with the lower nose-down pitching moment integral value seen in Table 6, as the rough-surface case is indeed found to exhibit lower loading in the rear part of the wing profile.

Figs. 21 and 22 are again figures of wing pressure distributions but in iso-lift conditions ($CL = 0.5$), aimed at a comparison against the available experimental data from the S1MA wind tunnel. Fig. 21 shows an overall good agreement between the elsA results and the experimental measurements, especially on the pressure side and for the internal wing sections. The details shown in Fig. 22 on the other hand better highlight the differences between the smooth-surface and rough-surface computations at the first three spanwise sections. Results at 28.3% span on the suction side and close to the leading edge show that accounting for both the surface roughness and the laminar flow up to 10% chord is really helpful in terms of reproducing the wind-tunnel test data. At the same spanwise section, a difference exists between the experimental and numerical *Cp* values in the vicinity of the shock wave, but it is clearly the AGC 7 µm with laminar flow case which exhibits the best agreement. The observations are similar on the suction side of the 50.2% wing section. Finally, the results at the 72.7% span section show that the reduced aft-loading due to the consideration of surface roughness in the computation leads to a better agreement with the experiments. The absence of surface roughness considerations might therefore be one of the reasons leading to the excessive aft-loading observed in numerical computations, an issue which has been widely discussed during the recent Drag Prediction Workshops.

Another interesting analysis concerns the intensity of the sources of drag generation along the spanwise direction for the different drag components. This can yield an improved insight on the impact of three-dimensional phenomena affecting the friction and viscous pressure drag coefficients, specifically with a focus on surface roughness in the present study. Fig. 23 presents the *CDf, CDvp*, and *CDw* curves for the three different cases NR, AGC 7 µm and AGC 7 µm with laminar flow up to 10% wing chord at $CL = 0.5$. This output can be interpreted as an approximate drag production over the aircraft span, the overall value of each component (Table 8) corresponding to the spanwise integral of the corresponding curve.

The very high values of the friction component in the first quarter of the span are due to the large wetted surface in this section, as it includes the fuselage, HTP, and VTP. The fully-turbulent AGC 7 µm simulation clearly produces stronger levels of *CDf* that are quite homogeneously distributed over the wing span. As already evoked, the laminar flow consideration on the rough-surface computation tends to give results

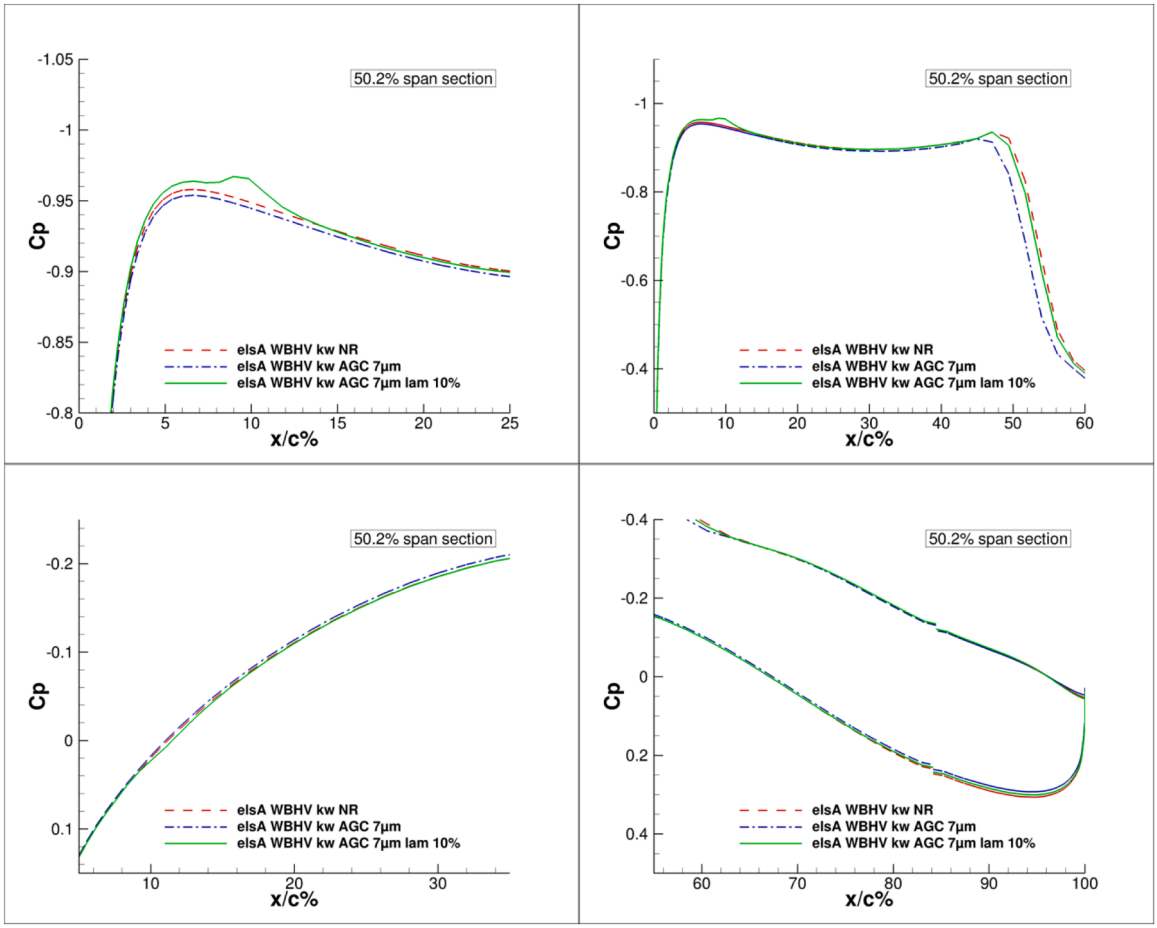

Fig. 20. *Cp* distributions, zoom on wing section $\eta = 50.2\%$; WBHV; S1MA conditions; $Ma = 0.85$, $Re(Lref(\text{S1MA})) = 4.65\times10^6$, iso-*alpha* = 2.75°.

closer to the smooth-surface case. As expected, the viscous pressure component is significantly larger in the fuselage sections for both rough-surface computations since this region always remains fully turbulent in this study. The impact of surface roughness on *CDvp* is clearly visible over the wing, but seems to decrease when moving towards the wing tip. The curves of spanwise production of wave drag *CDw* show a slight increase on the wing for the fully-turbulent rough-surface computation compared to the other cases, which is probably mainly due to the greater angle of attack needed to reach the target lift coefficient.

Coming back to variables typical of surface roughness studies, Fig. 24 shows a view of the roughness Reynolds number k_s^+ on the aircraft surface (computed with $k_{sTrans} = 7$ µm as explained in Sec. 4.2). The left figure shows the AGC rough-surface simulation and the right one represents the same but with the consideration of laminar flow at the wing leading edge. The corresponding friction Reynolds number defined as $Ref = (U\tau/\nu)^*\delta$ ranges from a few hundred at the wing leading edge, where the boundary layer is very thin, to around 5000 close to the trailing edge. Fig. 24 shows that the k_s^+ values on the S1MA model are relatively low and range roughly from 1 to 6. Similarly to the S8Ch study [14], such roughness Reynolds number values could have been considered as belonging to the hydrodynamically-smooth regime, but the computations and experiments are found to confirm the significant effect on drag compared to the smooth or mirror-polished surfaces. As expected, the areas of the wing and tail leading edges are the most impacted, thus exhibiting higher k_s^+ values, with a notable exception occurring when the laminar flow up to 10% chord on the wing induces a friction velocity reduction.

To conclude this part, it should be mentioned that some additional computations have been carried out in the S1MA conditions using the Wing-Body point-matched grids described in Sec. 3.2. As these grids have a much lower first-cell height, the objective was to investigate a potential Y^+ impact on the surface roughness effect. The average Y^+ is around 0.5 for the overset family of grids in these wind-tunnel conditions, and roughly ten times lower for the point-matched family of grids. The elsA results showed that this major difference in Y^+ values did not produce significant changes on the surface roughness effect.

5.3. Roughness effects with pressure sensitive paint

During a different campaign, tests were carried out in the S1MA wind tunnel in order to evaluate different PSP methods. One of these tests is here used to present a case with more pronounced surface roughness, although this is not representative of the state-of-the-art PSP test campaigns in S1MA. As discussed in Sec. 4.2 and following the outcomes of the S8Ch study, an equivalent sand-grain height of 15 µm will be used to calculate the model whose wings were painted and covered with talc. More precisely, only the wing of the numerical geometry is submitted to this value of 15 µm, while the rest (fuselage and tails) remains modeled with an equivalent grain sand-grain height of 7 µm.

The results of the elsA computations as well as the S1MA drag polar in presence of this PSP are given in Fig. 25. These confirm that surface roughness can have a substantial impact on aerodynamic performance. Once again, albeit being satisfactory, the agreement between the numerical drag polar with the equivalent height of 15 µm and the experimental data with PSP is not the main point of this particular comparison. The aim of the comparison is rather to highlight that the inclusion of surface roughness yields numerical computations which better reproduce the physics of the experiments. Both the numerical and

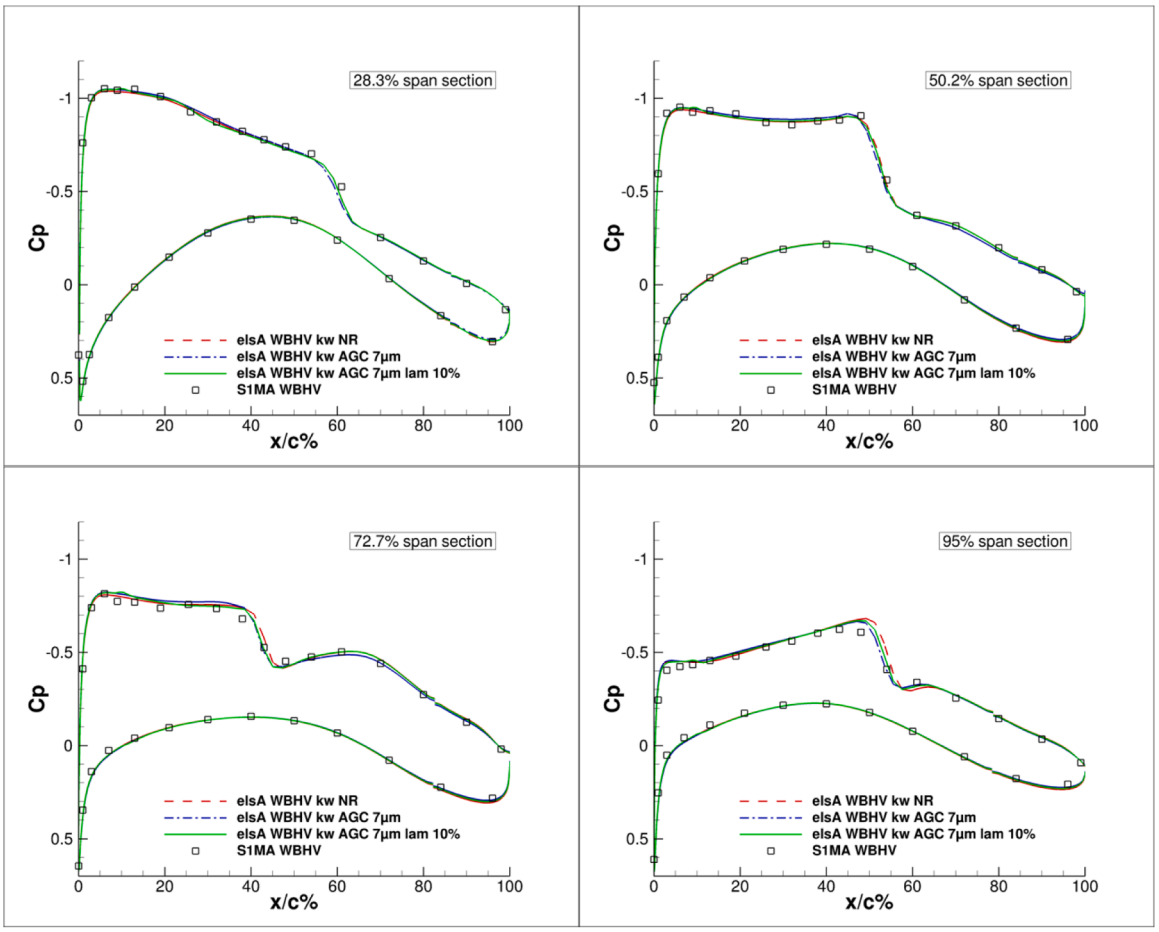

Fig. 21. *Cp* distributions on different wing sections; WBHV; S1MA conditions; $Ma = 0.85$, $Re(Lref(\text{S1MA})) = 4.65\times10^6$, iso-$CL = 0.5$.

wind tunnel data agree in terms of quantifying a drag increase due to the additional roughness on the wings of 5 counts for *CL* close to 0.4, about 10 counts for $CL = 0.5$ and 15 counts for $CL = 0.58$. As it will be discussed in the next paragraph, the Mach number value plays a role in this sensitivity to the lift coefficient.

5.4. Mach number effect

It was observed during some of the S1MA tests that the roughness effect could be sensitive to the Mach number value. As a consequence, additional computations at $Ma = 0.80$ and 0.87 have been included in order to better evaluate this sensitivity. The stagnation pressure is kept at $P_i = 89{,}000$ Pa, and the stagnation temperature is slightly adjusted around 323 K so that the Reynolds number is still 4.65×10^6. Fig. 26 presents the drag polars for the three Mach numbers. Only the elsA results of the smooth-surface (NR) and the rough-surface AGC 7 µm cases are given. It can be seen that for the lowest Mach number the difference between the NR and AGC curves is almost constant and equal to about 17 drag counts for CL = 0.44 and 18–19 counts for CL = 0.56. However, it is no longer the case for the Mach numbers 0.85 and 0.87. At $Ma = 0.85$ the drag penalty due to surface roughness is close to 18 counts at $CL = 0.44$ but close to 21 counts at $CL = 0.56$. At $Ma = 0.87$, the difference remains at about 18 counts for the lowest *CL* values, but becomes more significant at higher CL values (24 drag counts at $CL = 0.5$ and about 32 counts at $CL = 0.56$). For this aircraft model in transonic wind-tunnel conditions, the impact of surface roughness is augmented at greater Mach numbers when increasing the lift beyond a certain *Ma* value.

6. Comparisons in S2MA conditions

The configuration investigated in this section is still the WBHV CRM discretized by the overset family of grids, but dimensioned in accordance with the S2MA wind-tunnel model (scale 1/50). The aerodynamic conditions are the following: Mach number $Ma = 0.85$, stagnation temperature $T_i = 300$ K and stagnation pressure P_i varying from 91,000 to 190,000 Pa (Reynolds number effect).

6.1. From S1MA to S2MA

To compare the data of S2MA to the results previously obtained in S1MA, the stagnation pressure in the wind tunnel was pushed up to 190,000 Pa (see Fig. 6). This produces a Reynolds number based on the model reference length of about four million ($Re/\text{m} \sim 26\times10^6$). As a consequence, a difference exists between the S1MA and S2MA Reynolds numbers ($Re(Lref(\text{S1MA})) = 4.65\times10^6$ and $Re(Lref(\text{S2MA})) = 3.68\times10^6$), which is the reason why the S1MA and S2MA NR curves from the elsA solver do not exhibit the same agreement as they would at identical *Re* (see Figs. 27 and 28). In Fig. 28, it can be observed that this difference of about one million leads to a higher drag for the S2MA NR case (about 10 counts at $CL = 0.5$). This is not an issue in terms of evaluating the roughness effects in S2MA, neither in terms of comparison of these effects with S1MA.

To insist on the lift loss that was presented through Tables 5 and 6, Fig. 27 shows the lift polars in the two wind tunnels (dashed lines for S1MA, continuous lines for S2MA). Obtaining $CL = 0.5$ in S1MA requires augmenting the $alpha = 2.62°$ in the smooth-surface case to $alpha = 2.72°$ in the rough-surface simulation, representing therefore about

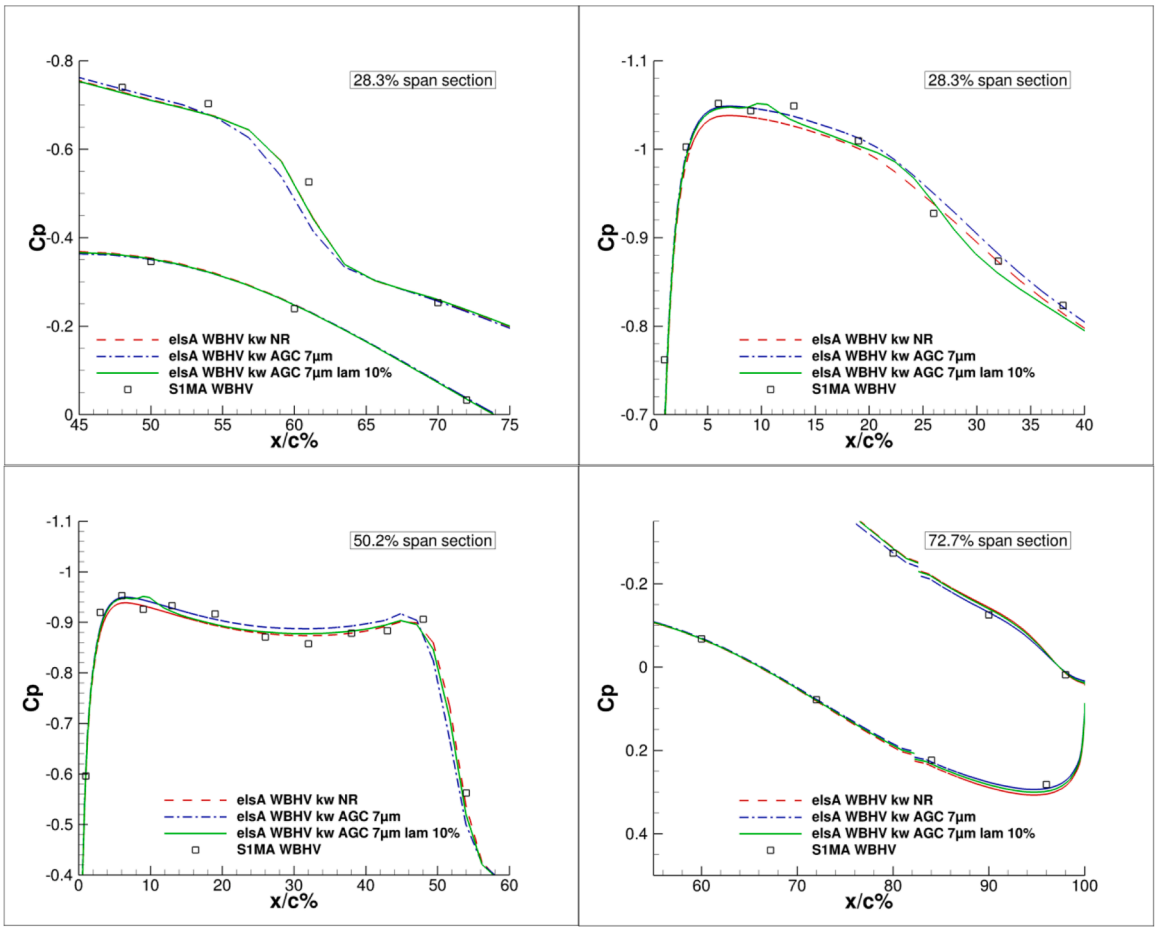

Fig. 22. *Cp* distributions, zoom on wing section $\eta = 50.2\%$; WBHV; S1MA conditions; $Ma = 0.85$, $Re(Lref(\text{S1MA})) = 4.65\times10^6$, iso-$CL = 0.5°$.

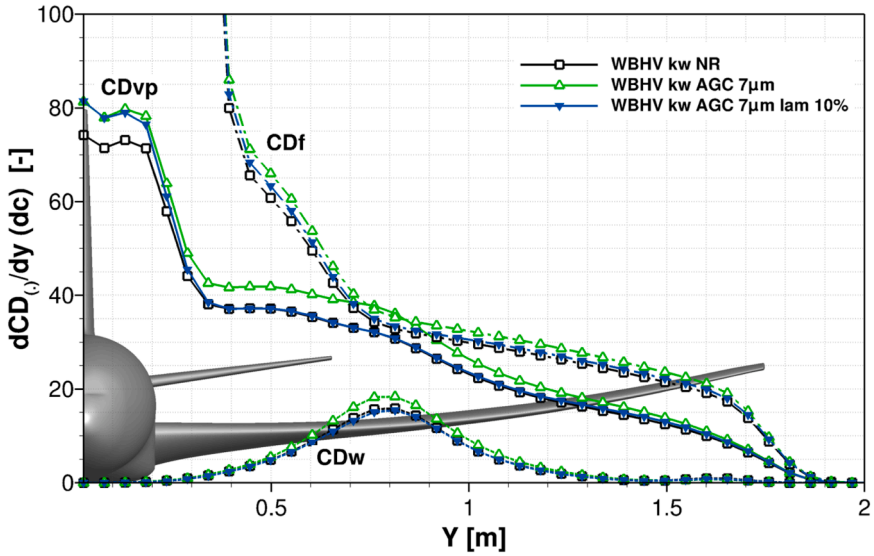

Fig. 23. *CDf, CDvp*, and *CDw* production along span; WBHV; S1MA conditions; $Ma = 0.85$, $Re(Lref(\text{S1MA})) = 4.65\times10^6$, $CL = 0.5$.

$+0.10°$ on the angle of attack to maintain the lift coefficient. In S2MA however, $CL = 0.5$ is obtained at an *alpha* of 2.68° without surface roughness and 2.91° with surface roughness, i.e. $+0.23°$, which is substantial. This figure shows that the roughness effect in S2MA conditions appears to be striking compared to what was observed in S1MA conditions.

Fig. 28 presents the drag polars of the NR, AGC 7 µm, and AGC 7 µm with laminar flow up to 10% chord computations, including the experimental data. It can be seen that for S2MA the agreement between the wind-tunnel curve and the elsA computation polar of the AGC 7 µm with laminar flow is not as good as in the case of S1MA. This probably means that the surface roughness of the S2MA model is indeed a bit

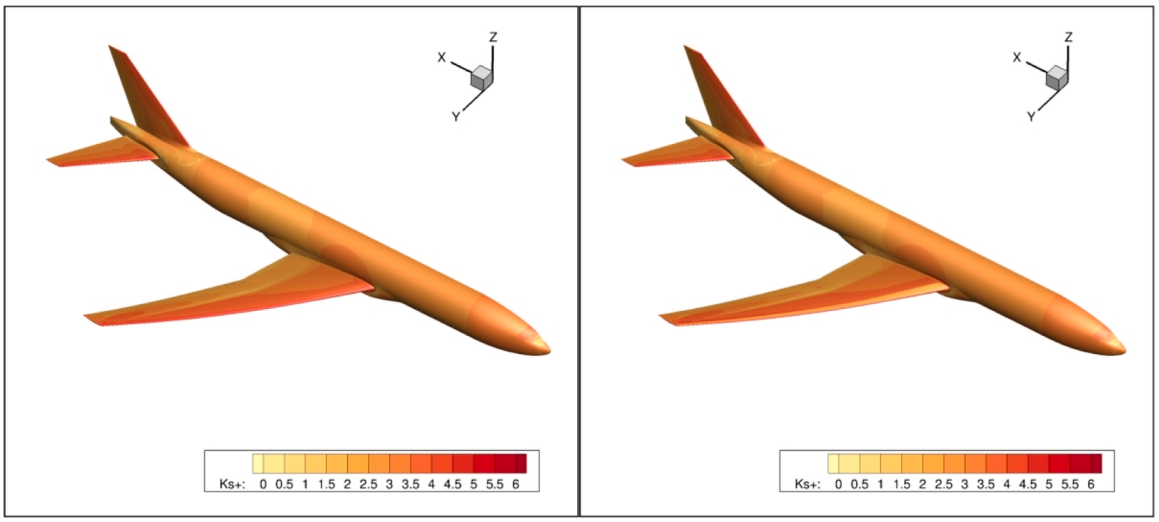

Fig. 24. k_s^+ distribution; WBHV; S1MA conditions; $Ma = 0.85$, $Re(Lref(\text{S1MA})) = 4.65\times10^6$, $alpha = 2.75°$; AGC 7 μm (left) and AGC 7 μm with laminar flow (right).

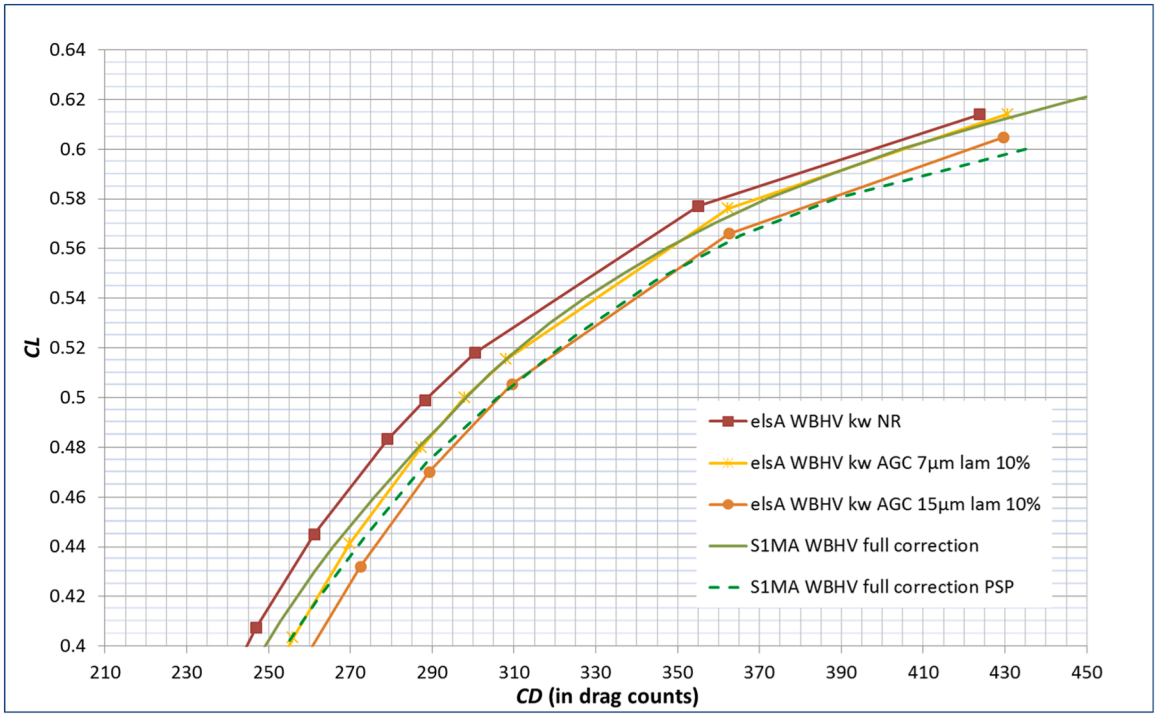

Fig. 25. Paint roughness effects; drag polars; WBHV; S1MA conditions; $Ma = 0.85$, $Re(Lref(\text{S1MA})) = 4.65\times10^6$.

better and that the equivalent sand-grain height value of 7 μm used in the solver is overestimated. What should however be highlighted is rather the variation of the surface roughness effect on drag between the two wind tunnels. In the S1MA conditions there exists a difference of about 10 drag counts between the elsA smooth-surface (NR) curve and the experiments at $CL = 0.5$ (initial observation mentioned in Sec. 1 and Sec. 5.1). Nonetheless, in S2MA this difference rises to 20 counts, which is now a significant discrepancy of about 6%. This is even more striking when considering the difference between the NR and AGC 7 μm numerical curves. In S1MA conditions, a difference of about +20 *dc* is predicted when passing from smooth-surface to rough-surface simulations, still for lift coefficient values close to 0.5, whereas in S2MAconditions the same difference exceeds +40 *dc*. Finally, the difference between the two wind-tunnel curves is about 20 to 30 drag counts along the polar. It is possible that about half of this difference is due to the lower Reynolds number in S2MA, but most of the rest is very likely due to roughness effects.

Indeed, even if the surface finish of the S2MA model is better than the one in S1MA, the greater Reynolds number per meter (26 million in S2MA versus 11 million) as well as the reduced model size (1/50 versus 1/16.835) are factors that tend to strengthen the roughness impact on lift and drag. Coarsely, the Reynolds number per meter is related to the thickness of the boundary layers developing on the wind-tunnel model, and the model size itself influences the portion of surface on which the ratio Ra/δ is large enough to generate effects. This can be confirmed by comparing Fig. 29 to Fig. 24 (S1MA), showing that the roughness Reynolds number k_s^+ distribution over the aircraft calculated with the same equivalent sand-grain height of 7 μm in both cases shows greater values in the S2MA conditions. These values were ranging from about 1 to 6 in S1MA conditions but reach values close to 10 in S2MA conditions,

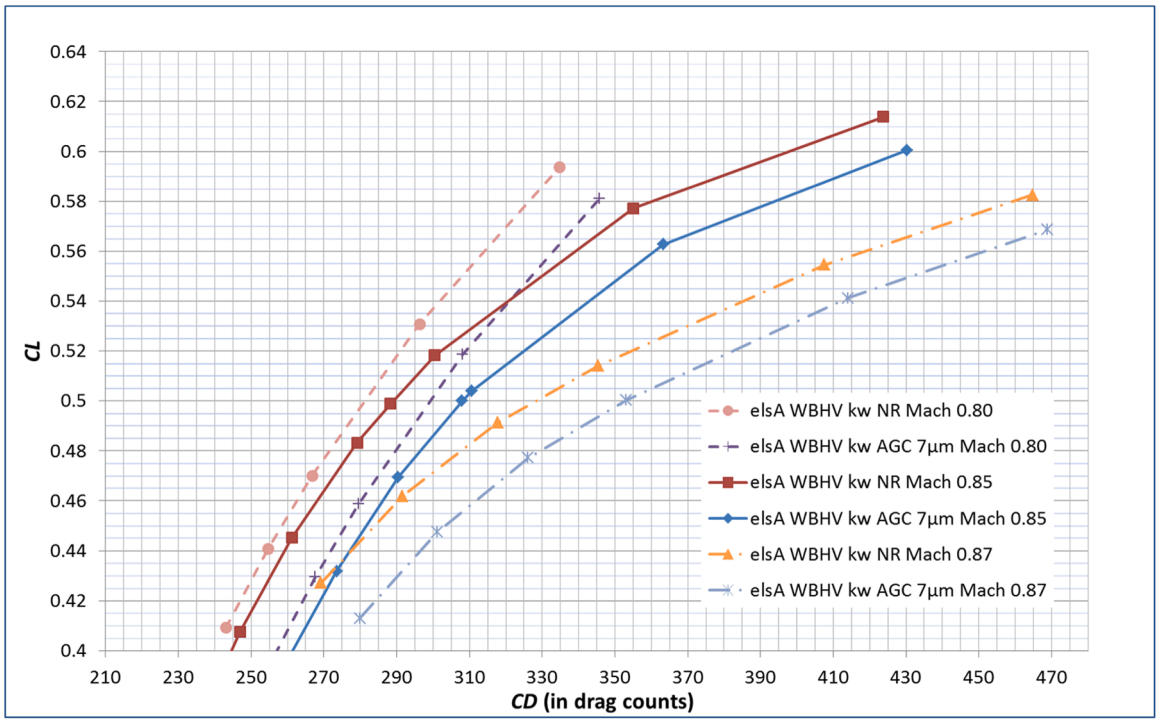

Fig. 26. Roughness effects with Mach number variation; drag polars; WBHV; S1MA conditions; $Ma = 0.80–0.87$, $Re(Lref(\text{S1MA})) = 4.65\times10^6$.

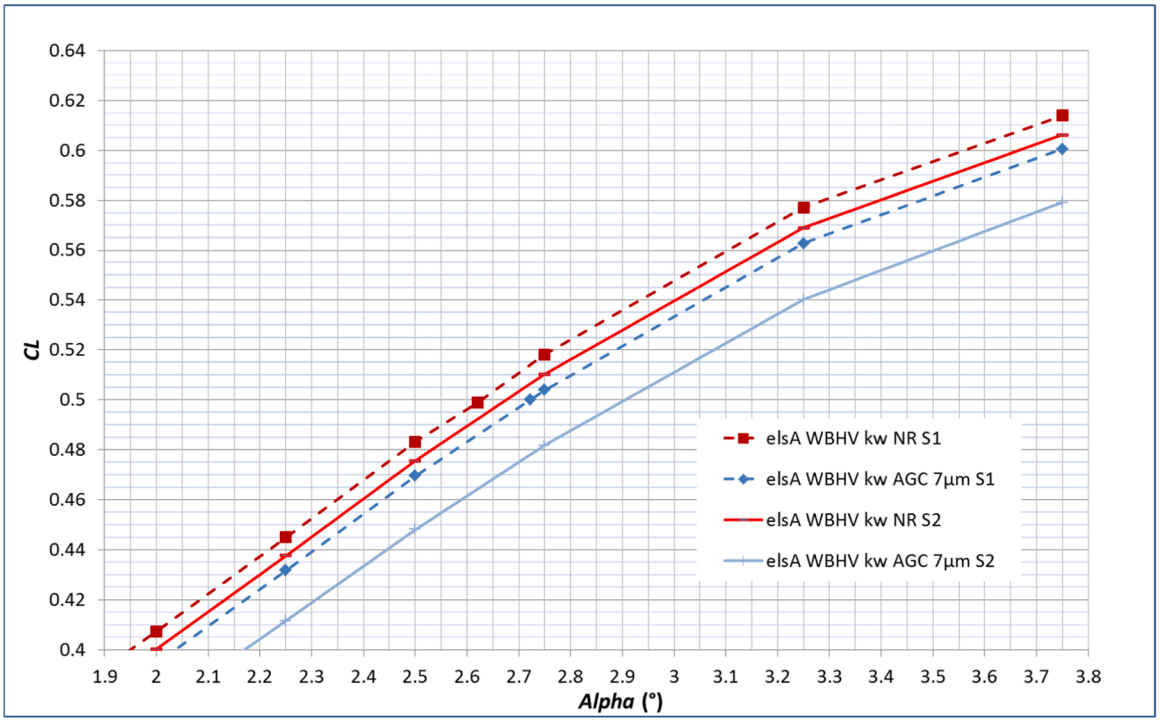

Fig. 27. Model surface roughness effects; lift polars; WBHV; S1MA and S2MA conditions; $Ma = 0.85$, $Re(Lref(\text{S1MA})) = 4.65\times10^6$ and $Re(Lref(\text{S2MA})) = 3.68\times10^6$.

clearly beyond the hydrodynamically-smooth regime, in agreement with the stronger roughness effects observed in S2MA.

6.2. Reynolds number effect

This paragraph aims at evaluating the gain of taking the surface roughness into account when computing a Reynolds number effect as it was carried out in experimental tests. During the S2MA campaign, the stagnation pressure P_i initially set at 190,000 Pa was reduced to 91,000 Pa, implying a Reynolds number decrease from 3.68 million to 1.76 million. This has been reproduced in the RANS simulations and shown in Fig. 30. The dashed lines stand for the reduced Reynolds number conditions. It should finally be mentioned that the numerical geometry used for the new computations is the same despite being possibly inappropriate in these lower-*Re* conditions, however the deltas can still be studied.

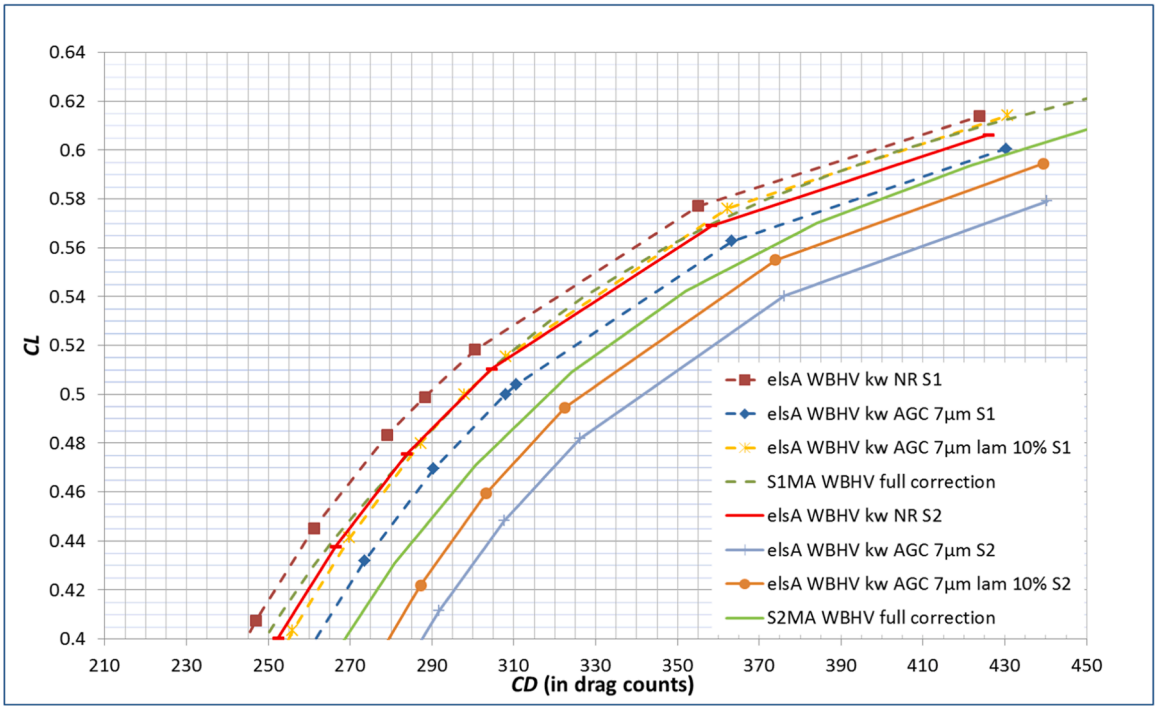

Fig. 28. Model surface roughness effects; drag polars; WBHV; S1MA and S2MA conditions; $Ma = 0.85$, $Re(Lref(\text{S1MA})) = 4.65\times10^6$ and $Re(Lref(\text{S2MA})) = 3.68\times10^6$.

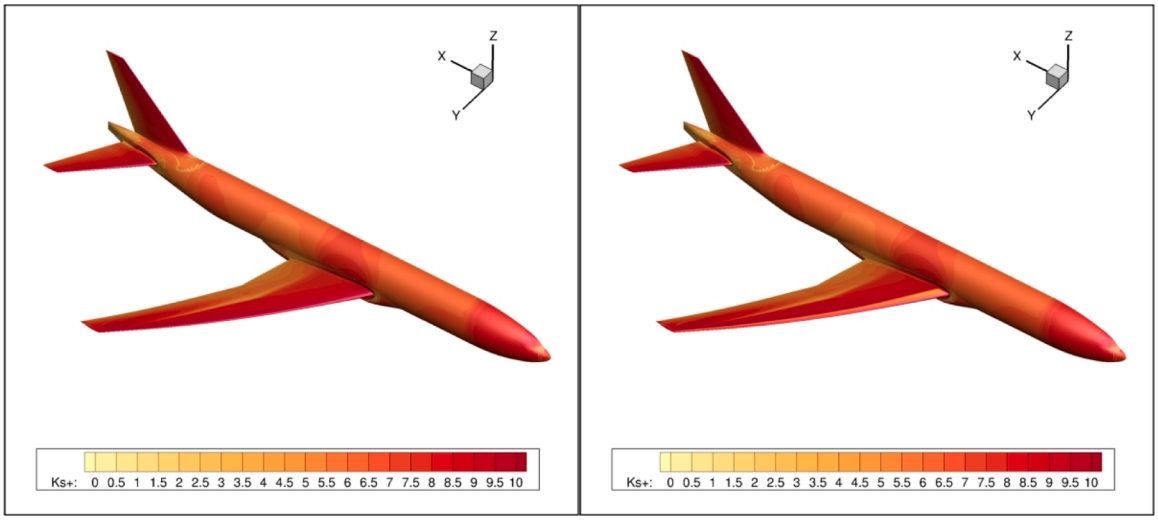

Fig. 29. k_s^+ distribution; WBHV; S2MA conditions; $Ma = 0.85$, $Re(Lref(\text{S2MA})) = 3.68\times10^6$, $alpha = 2.75°$; AGC 7 µm (left) and AGC 7 µm with laminar flow (right).

The difference between the two experimental polars is found to be about 17–18 drag counts at $CL = 0.5$, while the difference between the smooth-surface elsA curves is more than 30 counts. The numerical approach without surface-roughness considerations therefore clearly fails to reproduce the Reynolds number effect measured in the wind tunnel. Nevertheless, when accounting for surface roughness, the difference between the AGC 7 µm curves is close to 20 counts, in much better agreement with the experiments.

7. Roughness effects in flight conditions

The study of this section considers the Wing-Body configuration, described by the point-matched family of grids as discussed in Sec. 3. The aerodynamic conditions are the ones corresponding to the cruise flight at an altitude of 11 km: $Ma = 0.85$, stagnation pressure and temperature $P_i = 35{,}000$ Pa, $T_i = 245$ K ($P_{inf} = 0.22$ bar, $T_{inf} = -59$ °C), and Reynolds number based on *Lref* close to 44 million ($Re/\text{m} \sim 6 \times 10^6$). The computations are fully turbulent since the existence of a significant laminar zone is not expected in these conditions.

The objective here is not to analyze the absolute lift and drag values, because no flight test data is available to actually validate these assessments. It is rather to study the surface roughness effects, trends and potential gains. The surface finish of real civil transport aircraft may depend on many parameters (paint, age, operation area) but it seems that a reasonable range for *Ra* could be 2 to 5 micrometers. Following a simple Schaffler-type correlation (see Sec. 4.2), this would lead to equivalent sand-grain height values from about 20 to 50 micrometers.

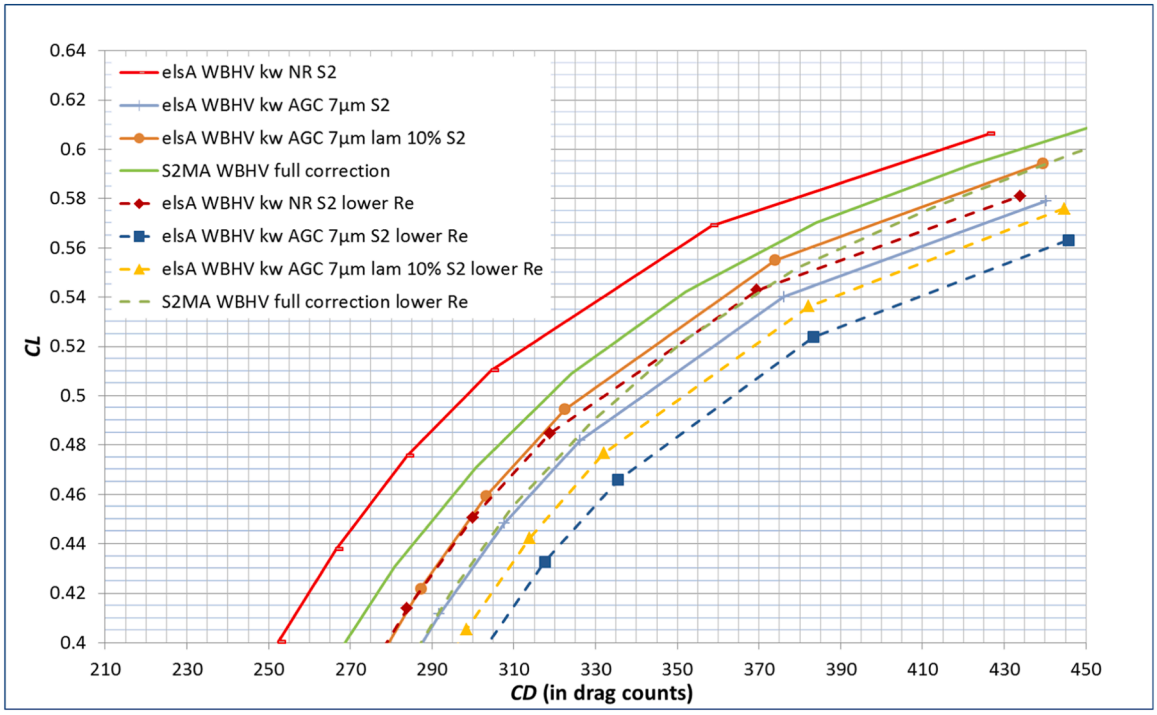

Fig. 30. Roughness effects with Reynolds number variation; drag polars; WBHV; S2MA conditions; $Ma = 0.85$, $Re(Lref(\text{S2MA})) = 1.76\times10^6$ and 3.68×10^6.

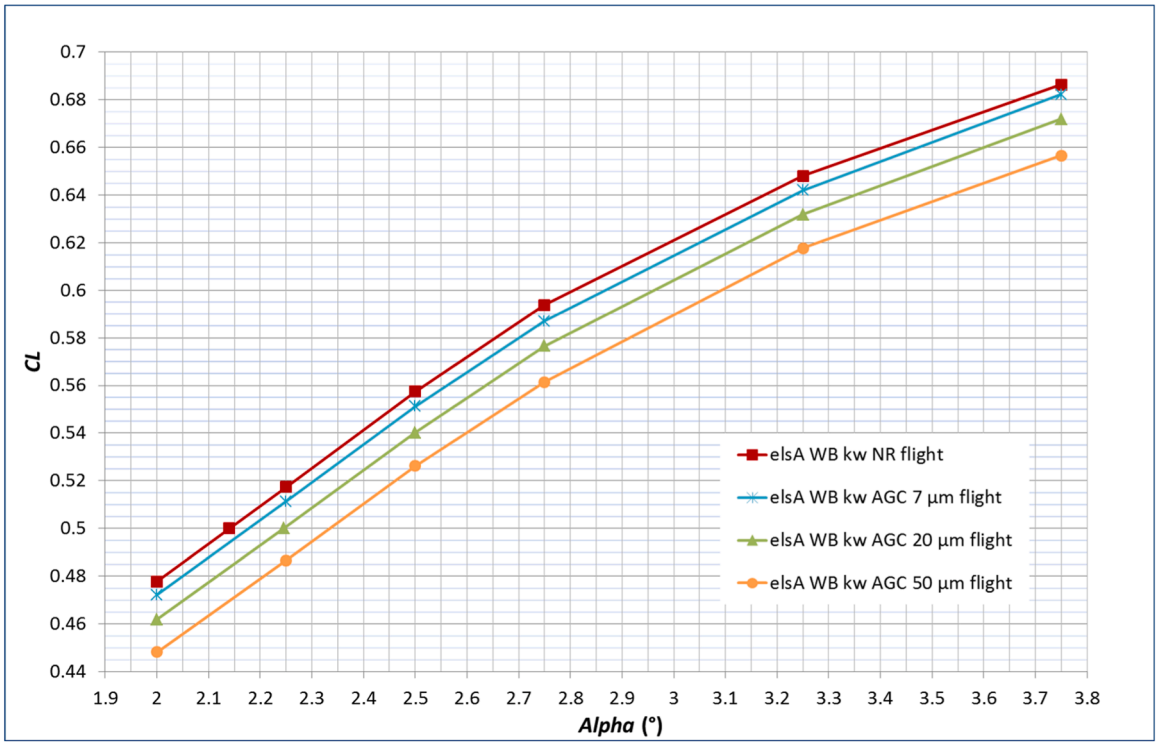

Fig. 31. Aircraft surface roughness effects; lift polars; WB; flight conditions; $Ma = 0.85$, $Re(Lref) = 44\times10^6$.

7.1. Global coefficients

The integral aerodynamic coefficients are presented in this paragraph. Fig. 31 shows the impact of surface roughness on the lift coefficient. A curve corresponding to an aircraft with perfectly-smooth surfaces (NR) is still presented for the sake of comparison against three surface roughness levels. The first corresponds to what was used for the S1MA and S2MA models ($Ra \sim 0.5$ µm, equivalent sand-grain height of 7 µm), which would mean a really smooth surface finish for a real aircraft in operation, the second is based on the lowest value of the roughness range given at the beginning of this section ($Ra \sim 2$ µm, equivalent sand-grain height of 20 µm), and the third is consistent with the highest value of the same roughness range ($Ra \sim 5$ µm, equivalent sand-grain height of 50 µm).

Similarly to the wind-tunnel conditions, the surface roughness is once again found to produce a significant impact on the *CL*(*alpha*) aircraft characteristics. The wing pressure distributions are affected in the same way as what was shown in Sec. 5.2, with a clear reduction of the lift production being noted on the suction and pressure sides, as well as a shock wave displacement towards the leading edge. The lift coefficient value of 0.5 is obtained at an angle of attack of 2.14° with the theoretical perfectly-smooth geometry. On the other hand, the $Ra \sim 2$ μm case requires an angle of attack of about 2.25°, which goes up to 2.34° for the roughest-surface case (thus between +0.11° and +0.20° to maintain the same lift). Another way to describe this effect is to consider a fixed angle of attack. At 2.25° the roughest surface generates a lift coefficient of only 0.487, the $Ra \sim 2$ μm case reaches $CL = 0.5$, the surface whose *Ra* is close to 0.5 μm produces 0.511, and the perfectly smooth aircraft gives $CL = 0.517$.

Fig. 32 then provides the drag polars of the different cases presented above. In these flight conditions with a lower *Re*/m value and a much larger "model" size compared to the wind tunnels, the roughness effect is reduced. Close to $CL = 0.5$, the difference between the NR and the AGC 7 μm curves is about 5 drag counts, while the same difference was about 20 dc in S1MA and 40 dc in S2MA (see Fig. 17 and Fig. 28). Although reduced with respect to the wind-tunnel conditions, this difference can still be far from being negligible. Indeed, if the cruise point is considered, the perfectly-smooth surface is associated to a drag value close to 206 counts, the 0.5 μm case to about 212 dc, the 2 μm geometry to 220 dc (i.e. +7%), and the 5 μm case generates a drag coefficient of 230 counts (+12%). Since a perfectly-smooth surface would be unachievable in practice, choosing the 0.5 μm surface roughness as a reference leads to the drag penalties for the 2 μm and 5 μm cases being significant (+4% and +8% respectively). These percentages of increase, which remain similar for greater lift coefficients close to 0.6, give an estimate of possible gains by a reduction of the surface roughness of aircraft in operation.

The near-field and far-field drag coefficients for the perfectly-smooth surface and the one with a roughness variable *Ra* of 2 μm are presented in Table 9 at $CL = 0.5$. This level of roughness can be considered as intermediate and can provide interesting evaluations of drag increase due to this mechanism. As discussed above, this surface produces a total drag 7% greater than the one of the theoretically-smooth geometry. About 46% of that increase is due to the friction component, and 40% comes from the viscous pressure coefficient. Beyond the surface roughness effects, and mainly due to the Reynolds number increase, comparing these figures with Table 8 shows that although the friction component was found to represent 46–47% of total drag in S1MA it is only 35–36% in the present case. In addition, the portion corresponding to the lift-induced drag coefficient was 30–32%, in comparison to 45.5–48% in flight conditions. The spurious drag for these grids is not as low as for the WBHV overset grid family, but still remains below the drag count and thus very satisfactory in terms of drag prediction accuracy.

7.2. Local analyses

As the viscous phenomena, and especially the skin friction, are mainly responsible for the drag increase due to surface roughness, it is of

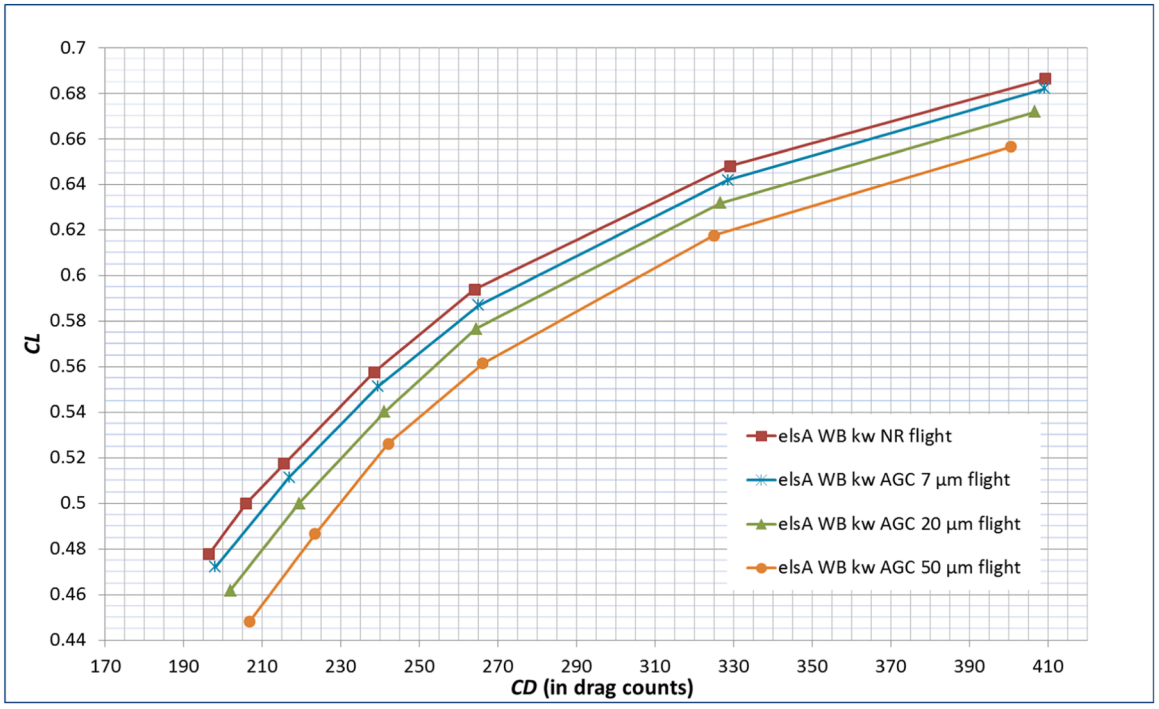

Fig. 32. Aircraft surface roughness effects; drag polars; WB; flight conditions; $Ma = 0.85$, $Re(Lref) = 44 \times 10^6$.

Table 9
k-ω SST; NR versus AGC 20 μm; near and far-field coefficients; WB; flight conditions; $Ma = 0.85$, $Re(Lref) = 44 \times 10^6$, $CL = 0.5$.

	CDp	*CDf*	*CDvp*	*CDv*	*CDw*	*CDi*	*CDff*
WB flight NR	133.4	72.4	30.8	103.2	3.6	98.6	205.4
% of *CDff*	64.9	35.2	15.0	50.2	1.8	48.0	100.0
WB flight AGC 20 μm	141.2	78.6	36.2	114.8	4.5	99.7	219.0
% of *CDff*	64.5	35.9	16.5	52.4	2.1	45.5	100.0
Delta AGC 20 μm - NR	7.8	6.2	5.4	11.6	0.9	1.1	13.6

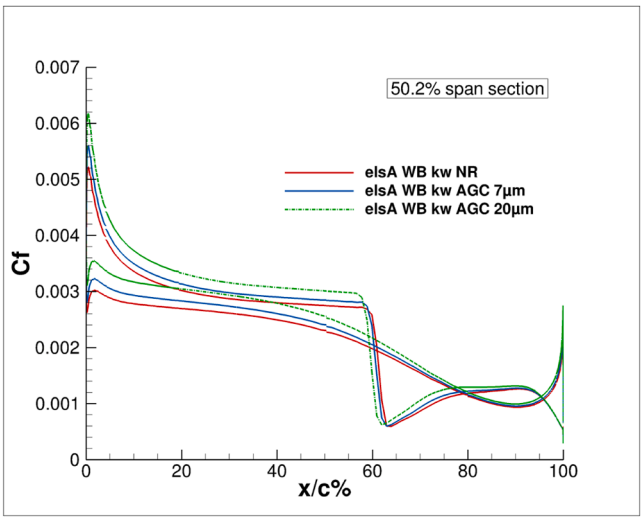

Fig. 33. *Cf* coefficient on wing section $\eta = 50.2\%$; WB; flight conditions; $Ma = 0.85$, $Re(Lref) = 44\times10^6$, iso-*alpha* $= 2.75°$.

interest to analyze coefficient distributions on the wing at flight conditions for CRM geometries exhibiting different surface roughness levels. Fig. 33 shows the *Cf* coefficient at 50.2% span for the perfectly-smooth surface as well as the ones with *Ra* values of 0.5 and 2 µm, all of them corresponding to an angle of attack of 2.75°. The observed behavior is very similar to the simulations performed at the S1MA conditions and presented in Fig. 18 (left). This confirms that if drag reduction is sought by reducing the roughness effects, then the effort could be focused on improving the wing surface finish over the first half of the profile. Both the pressure and suctions sides offer a potential benefit.

At this point a comparison should be made with the studies and projects involving aircraft equipped with laminar wings [49], for some of which the total drag reduction can be substantial (10–15%). The laminar flow technology is naturally based on a more unstable mechanism, since there exist multiple reasons for which a laminar boundary layer over an aircraft in operation is subject to become turbulent and introduce a significant drag increase. On the other hand, the benefit from smoother aircraft surfaces might be more difficult to achieve but lies in the turbulent regime and therefore could ensure more robustness.

As in the section dedicated to the results in the S1MA wind tunnel and especially Fig. 23, a comparison of the spanwise drag productions between the smooth-surface geometry and a rough-surface one exhibiting *Ra* values close to 2 µm is shown in Fig. 34. The effects of surface roughness in flight conditions are very similar to what was observed at the S1MA conditions. In particular, these effects involve a friction drag increase quite uniformly distributed over the wing, greater viscous pressure drag especially in the fuselage region because of the larger wetted surface, and stronger shock wave drag close to mid-span due to the increased angle of attack required to maintain $CL = 0.5$ with the rough surface.

Following these far-field analyses, it is also important to position the roughness Reynolds numbers obtained in flight conditions so that they can be compared to the corresponding values at wind-tunnels conditions. Fig. 35 shows the k_s^+ distribution for the surfaces with $Ra = 0.5$ µm at left and $Ra = 2$ µm at right. A comparison of these results against Fig. 24 and Fig. 29 shows that the k_s^+ values of the 2 µm-*Ra* surface are greater than the ones of the S1MA model and not far from the ones of S2MA, in which the observed roughness effects were found to be significant.

8. Conclusions and perspectives

This study was aimed at investigating the surface roughness effects on transonic aircraft performance. The objectives were to evaluate the need to consider the roughness of wind-tunnel models in experimental tests, to propose a way of taking it into account in RANS computations, and to extend these observations to the full-scale geometry in flight conditions.

The Common Research Model configuration, representative of modern civil aircraft, was used as a reference for the study. This was carried out by using some of the grids provided in the framework of the international Drag Prediction Workshop in order to perform CFD simulations reproducing recent ONERA experimental testing campaigns which took place in the large S1MA and S2MA wind tunnels.

The surface roughness of the CRM models, whose surface finish exhibited average roughness variables *Ra* close to 0.5 µm, was considered in the solver through an equivalent sand-grain height k_s approach. The latter was obtained from a Musker-type correlation involving surface roughness characteristics such as *Rq* (RMS roughness height), *Sk* and *Ku* (skewness and kurtosis coefficients) and *Sp* (slope parameter).

The difference between the perfectly-smooth computation and the S1MA data (corrected for wall and support effects) was found to be about 10 drag counts at the cruise point. On the other hand, taking the surface roughness of the wind-tunnel model into account in the CFD, as

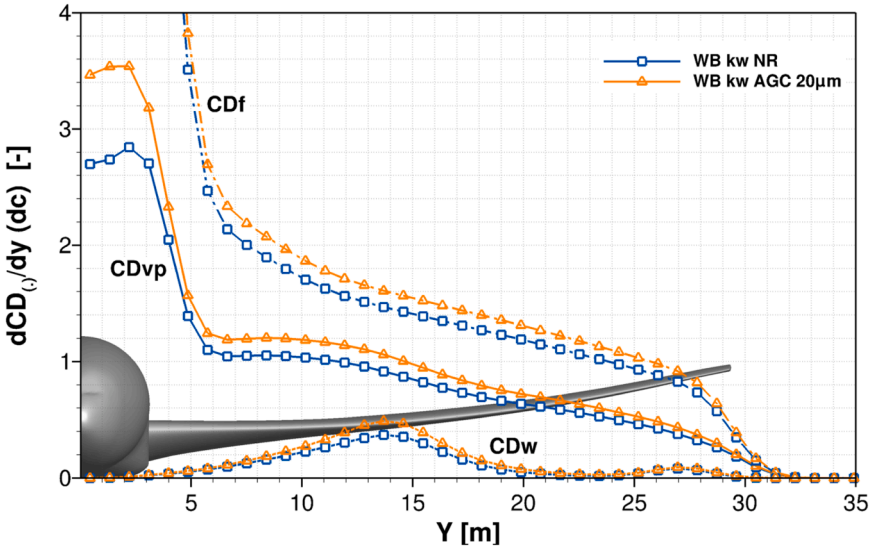

Fig. 34. *CDf*, *CDvp*, and *CDw* production along span; WB; flight conditions; $Ma = 0.85$, $Re(Lref(\text{S1MA})) = 4.65\times10^6$, $CL = 0.5$.

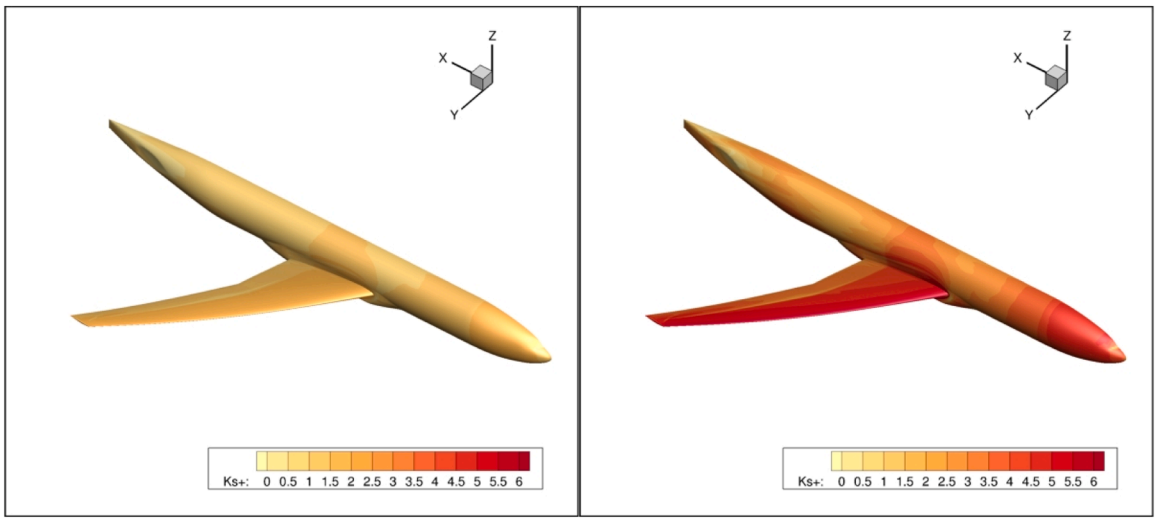

Fig. 35. k_s^+ distribution; WB; flight conditions; $Ma = 0.85$, $Re(Lref) = 44\times10^6$, $alpha = 2.75°$; AGC 7 μm (left) and AGC 20 μm (right).

well as introducing laminar flow up to 10% of wing chord (as in the experiment), allowed an almost perfect agreement to be achieved over a large portion of the drag polar *CL*(*CD*). The impact of surface roughness on lift, wing pressure distributions, near-field and far-field drag coefficients was found to be significant, for example corresponding to +6–7% on the total drag for lift coefficients up to 0.5 (56% from friction, 33% from viscous pressure). Moreover, it was shown that beyond a certain Mach number value, the greater the Mach number is, the greater the roughness effect will be when increasing the lift.

The test campaign in S2MA demonstrated that the surface roughness effects can also affect the comparison between wind tunnels. The Reynolds number per meter and the model size play a decisive role in the way the aerodynamic coefficients are impacted. The difference between the smooth-surface computation and the S2MA measurements reaches 20 drag points close to $CL = 0.5$, which is two times greater than in S1MA.

As a conclusion, the results of the present study clearly indicate that the surface roughness must be considered in CFD computations which are carried out for comparisons against experimental data, for pre-testing studies, or even for accurate aircraft design, if absolute lift and drag values are needed. Surface roughness effects should also be considered before the wind-tunnel model production in order to determine the surface finish characteristics consistent with the targeted *Re*/m and test objectives.

Furthermore, when dealing with the full-scale aircraft in cruise conditions at high altitude, the computations showed that an aircraft surface whose *Ra* is about 2 μm would produce a drag coefficient 4% greater than the one of a surface exhibiting *Ra* values around 0.5 μm. The gain achievable with smoother surfaces might be limited compared to laminar flow technologies, but could be more robust for real aircraft in operation. Moreover, the effort on achieving a very smooth surface finish may be focused only on the most relevant parts of the geometry. This could provide a basis for more refined investigations and developments among aircraft manufacturers and airlines in the pursuit of a lower environmental impact of the worldwide air traffic.

CRediT authorship contribution statement

David Hue: Writing – review & editing, Writing – original draft, Visualization, Methodology, Investigation, Formal analysis, Data curation. **Aurélia Cartieri:** Writing – review & editing, Writing – original draft, Visualization, Methodology, Investigation, Formal analysis, Data curation. **Ilias Petropoulos:** Writing – review & editing, Writing – original draft, Validation, Software, Methodology.

Declaration of competing interest

The authors declare that they have no known competing financial interests or personal relationships that could have appeared to influence the work reported in this paper.

Data availability

The authors do not have permission to share data.

Acknowledgments

The authors thank Pascal Molton for the surface roughness study in S8Ch, Olivier Atinault for having shared his expertise in the field of drag prediction, and Michaël Méheut for his constant support of such research studies. The work presented in this article has been funded with general resources of ONERA.

References

[1] A. Cartieri, D. Hue, Q. Chanzy, O. Atinault, Experimental investigations on common research model at ONERA-S1MA – drag prediction workshop numerical results, J. Aircr. 55 (4) (2018) 1491–1508, https://doi.org/10.2514/1.C034414. July–August.
[2] Vassberg, J.C., DeHann, M.A., Rivers, S.M., Wahls, R.A., "Development of a common research model for applied CFD validation studies," AIAA Paper 2008-6919, 2008, https://doi.org/10.2514/6.2008-6919.
[3] Drag Prediction Workshop website, https://aiaa-dpw.larc.nasa.gov. Accessed in September 2023.
[4] Journal of Aircraft, Special section: "drag prediction workshops IV and V", Vol. 51, No. 4, July.-August. 2014, pp. 1069–1343, https://doi.org/10.2514/1.C033081.
[5] F.R. Menter, Two-equation eddy-viscosity turbulence models for engineering applications, AIAA Journal 32 (8) (August 1994) 1598–1605, https://doi.org/10.2514/3.12149.
[6] D.C. Wilcox, Reassessment of the scale-determining equation for advanced turbulence models, AIAA Journal 26 (11) (1988) 1299–1310, https://doi.org/10.2514/3.10041.
[7] J.P. Bons, A review of surface roughness effects in gas turbines, J. Turbomach. 132 (2) (2010) 021004, https://doi.org/10.1115/1.3066315.
[8] T.O. Jelly, W. Abu Rowin, N. Hutchins, D. Chung, K. Tanimoto, T. Oda, R. D. Sandberg, High-fidelity computational assessment of aero-thermal performance and the reynolds' analogy for additively manufactured anisotropic surface roughness, J. Turbomach. 145 (11) (2023) 111005, https://doi.org/10.1115/1.4063298.
[9] S. Meynet, A. Barge, V. Moureau, G. Balarac, G. Lartigue, A. Hadjadj, Roughness-resolved large-eddy simulation of additive manufacturing-like channel flows, J. Turbomach. 145 (8) (2023) 081013, https://doi.org/10.1115/1.4062245.
[10] F. Chedevergne, A double-averaged Navier-Stokes k–ω turbulence model for wall flows over rough surfaces with heat transfer, J. Turbulence 22 (11) (2021) 713–734, https://doi.org/10.1080/14685248.2021.1973014.

[11] B. Aupoix, Roughness corrections for the k–ω shear stress transport model: status and proposals, ASME J. Fluids Eng. (February 2015), https://doi.org/10.1115/1.4028122.
[12] E. Croner, O. Léon, F. Chedevergne, Industrial use of equivalent sand grain height models for roughness modelling in turbomachinery, in: Paper FP10-2020, 55th 3AF International Conference on Applied Aerodynamics, Poitiers, France, March 2020. https://hal.science/hal-03228846/.
[13] M. Kadivar, D. Tormey, G. McGranaghan, A review on turbulent flow over rough surfaces: fundamentals and theories, Int. J. Thermofluids 10 (2021) 100077, https://doi.org/10.1016/j.ijft.2021.100077.
[14] D. Hue, P. Molton, Turbulent drag induced by low surface roughness at transonic speeds: experimental/numerical comparisons, Phys. Fluids 32 (4) (2020), https://doi.org/10.1063/1.5143068.
[15] J. Nikuradse, Laws of flow in rough pipes, NACA Tech. Memorandum 1292 (1950).
[16] C.F. Colebrook, Turbulent flow in pipes with particular reference to the transition between smooth and rough pipe laws, J. Inst. Civ. Eng. 11 (1939) 133, https://doi.org/10.1680/ijoti.1939.13150.
[17] L.F. Moody, Friction factors for pipe flow, Trans. ASME 66 (1944), https://doi.org/10.1115/1.4018140, 671.
[18] J. Jiménez, Turbulent flows over rough walls, Ann. Rev. Fluid Mech. 36 (2004) 173–196, https://doi.org/10.1146/annurev.fluid.36.050802.122103.
[19] K.A. Flack, M.P. Schultz, Roughness effects on wall-bounded turbulent flows, Phys. Fluids 26 (October 2014), https://doi.org/10.1063/1.4896280.
[20] J. Yuan, U. Piomelli, Estimation and prediction of the roughness function on realistic surfaces, J. Turbulence 15 (6) (2014) 350–365, https://doi.org/10.1080/14685248.2014.907904.
[21] M. Thakkar, A. Busse, N.D. Sandham, Direct numerical simulation of turbulent channel flow over a surrogate for Nikuradse-type roughness, J. Fluid. Mech. 837 (2018) R1, https://doi.org/10.1017/jfm.2017.873.
[22] D. Chung, N. Hutchins, M.P. Schultz, K.A. Flack, Predicting the Drag of Rough Surfaces, Annu Rev. Fluid. Mech. 53 (2021) 439–471, https://doi.org/10.1146/annurev-fluid-062520-115127.
[23] A.J. Musker, Universal roughness functions for naturally-occurring surfaces, Trans. Can. Soc. Mech. Eng. 6 (1) (1980), https://doi.org/10.1139/tcsme-1980-0001.
[24] M.P. Schultz, K.A. Flack, Turbulent boundary layers on a systematically varied rough wall, Phys. Fluids 21 (January 2009), https://doi.org/10.1063/1.3059630.
[25] Tinoco, E.N., Brodersen, O., Keye, S., Laflin, K., Vassberg, J.C., Rider, B., Wahls, R. A., Morrison, J.H., Pomeroy, B.W., Hue, D., Murayama, M., "Summary data from the seventh AIAA CFD drag prediction workshop," AIAA Paper 2023-3492, 2023, https://doi.org/10.2514/6.2023-3492.
[26] Common Research Model website, http://commonresearchmodel.larc.nasa.gov/. Accessed in September 2023.
[27] ETW CRM campaign website, https://w3.onera.fr/ESWIRP-TNA-ETW-CRM-2014/. Accessed in September 2023.
[28] D. Hue, S. Esquieu, Computational drag prediction of the DPW4 configuration using the far-field approach, J. Aircr. 48 (5) (Sept.-Oct. 2011) 1658–1670, https://doi.org/10.2514/1.C031337.
[29] D. Hue, Fifth drag prediction workshop: ONERA investigations with experimental wing twist and laminarity, J. Aircr. 51 (4) (2014) 1311–1322, https://doi.org/10.2514/1.C032438. July.-August.
[30] D. Hue, Q. Chanzy, S. Landier, DPW-6: drag analyses and increments using different geometries of the common research model airliner, J. Aircr. 55 (4) (2018) 1509–1521, https://doi.org/10.2514/1.C034139. July–August.
[31] D. Hue, F. Sartor, I. Petropoulos, C. Fournis, DPW-7: steady and unsteady computations of the common research model at different reynolds numbers, J. Aircr. 60 (6) (November-December 2023) 1857–1871, https://doi.org/10.2514/1.C037231.
[32] D. Hue, S. Péron, L. Wiart, O. Atinault, E. Gournay, P. Raud, C. Benoit, J. Mayeur, Validation of a near-body and off-body grid partitioning methodology for aircraft aerodynamic performance prediction, Comput. Fluids 117 (Aug. 2015) 196–211, https://doi.org/10.1016/j.compfluid.2015.05.021.
[33] Le Sant, Y., Mignosi, A., Touron, G., Deléglise, B., Bourguignon, G., "Model deformation measurement (MDM) at ONERA", 25th AIAA applied aerodynamics conference, AIAA 2007-3817, Miami, 25–28, June 2007, https://doi.org/10.2514/6.2007-3817.
[34] X. Vaucheret, Recent Calculation Progress on Wall Interferences in Industrial Wind Tunnels, La Recherche Aérospatiale 3 (1988) 45–47.
[35] Pistolesi, E., "Collected lectures of the principal meeting of the Lilienthal society", Considering respecting the mutual influence of system of airfoils, Berlin, 1937.
[36] A. Cartieri, S. Mouton, Using CFD to calculate support interference effects, in: 28th Aerodynamic Measurement Technology, Ground Testing, and Flight Testing Conference, New Orleans, Louisiana, 2012, https://doi.org/10.2514/6.2012-2864. AIAA Paper 2012-2864.
[37] DPW-6 overset grids, https://dpw.larc.nasa.gov/DPW6/overset_grids_Boeing_Serrano.REV00/. Retrieved in June 2023.
[38] C. Benoit, S. Péron, S. Landier, Cassiopee: a CFD pre- and post-processing tool, Aerosp. Sci. Technol. 45 (September 2015) 272–283, https://doi.org/10.1016/j.ast.2015.05.023.
[39] DPW-7 point-matched grids, https://dpw.larc.nasa.gov/DPW7/Vassberg_Grids.REV00/LoQ/. Retrieved in July 2023.
[40] L. Cambier, S. Heib, S. Plot, The ONERA elsA CFD Software: input from Research and Feedback from Industry, Mech. Ind. 15 (3) (2013) 159–174, https://doi.org/10.1051/meca/2013056.
[41] Jameson, A., Schmidt, W., and Turkel, E., "Numerical solution of the euler equations by finite volume methods using runge kutta time stepping schemes," AIAA Paper 81-1259, June 1981, https://doi.org/10.2514/6.1981-1259.
[42] Spalart, P.R., and Allmaras, S.R., "A one-equation turbulence model for aerodynamic flows," AIAA Paper 92-0439, 1992, https://doi.org/10.2514/6.1992-439.
[43] P.R. Spalart, Strategies for turbulence modelling and simulation, Int. J. Heat. Fluid. Flow. 21 (2000) 252–263, https://doi.org/10.1016/S0142-727X(00)00007-2.
[44] A. Schäffler, Experimental and analytical investigation of the effects of reynolds number and blade surface roughness on multistage axial flow compressors, ASME J. Eng. Power 102 (1980) 5–13, https://doi.org/10.1115/1.3230232.
[45] D. Destarac, Far-Field / Near-Field Drag Balance and Applications of Drag Extraction in CFD, CFD-Based Aircraft Drag Prediction and Reduction, VKI Lecture Series, 2003-02, von Karman Institute for Fluid Dynamics, Rhode-Saint-Genèse, Belgium 3-7 November 2003.
[46] D. Destarac, J. Van Der Vooren, Drag/thrust analysis of jet-propelled transonic transport aircraft; definition of physical drag components, Aerosp. Sci. Technol. 8 (6) (2004) 545–556, https://doi.org/10.1016/j.ast.2004.03.004.
[47] D. Bailly, I. Petropoulos, C. Wervaecke, M. Méheut, O. Atinault, C. Fournis, An overview of ONERA research activities related to drag analysis and breakdown, AIAA Paper (2021) 2021–2551, https://doi.org/10.2514/6.2021-2551.
[48] C. Fournis, I. Petropoulos, F. Sartor, Unsteady far-field drag analyses of transonic buffet over the NASA common research model, in: Paper AERO2023-24, 57th 3AF International Conference on Applied Aerodynamics, Bordeaux, France, March 2023. https://hal.science/hal-04065886.
[49] D. Hue, O. Vermeersch, J. Duchemin, O. Colin, D. Tran, Wind-tunnel and CFD investigations focused on transition and performance predictions of laminar wings, AIAA Journal 56 (1) (January 2018) 132–145, https://doi.org/10.2514/1.J056088.